

DETECTION OF THE SPLASHBACK RADIUS AND HALO ASSEMBLY BIAS OF MASSIVE GALAXY CLUSTERS

SURHUD MORE¹, HIRONAO MIYATAKE^{2,3,1}, MASAHIRO TAKADA¹, BENEDIKT DIEMER⁴, ANDREY V. KRAVTSOV^{5,6,7}, NEAL K. DALAL^{8,1}, ANUPREETA MORE¹, RYOMA MURATA^{1,9}, RACHEL MANDELBAUM¹⁰, EDUARDO ROZO¹¹, ELI S. RYKOFF¹², MASAMUNE OGURI^{9,13,1}, DAVID N. SPERGEL^{3,1}

¹ Kavli Institute for the Physics and Mathematics of the Universe (WPI), Tokyo Institutes for Advanced Study, The University of Tokyo, 5-1-5 Kashiwanoha, Kashiwa-shi, Chiba, 277-8583, Japan; surhud.more@ipmu.jp

² Jet Propulsion Laboratory, California Institute of Technology, Pasadena, CA 91109, USA

³ Department of Astrophysical Sciences, Princeton University, Peyton Hall, Princeton NJ 08544 USA

⁴ Harvard-Smithsonian Center for Astrophysics, 60 Garden St., Cambridge, MA 02138 USA

⁵ Department of Astronomy and Astrophysics, The University of Chicago, Chicago, IL 60637 USA

⁶ Kavli Institute for Cosmological Physics, The University of Chicago, Chicago, IL 60637 USA

⁷ Enrico Fermi Institute, The University of Chicago, Chicago, IL 60637 USA

⁸ Department of Physics, University of Illinois Urbana-Champaign, 1110 West Green Street Urbana, IL 61801-3080 USA

⁹ Department of Physics, University of Tokyo, 7-3-1 Hongo, Bunkyo-ku, Tokyo 113-0033 Japan

¹⁰ McWilliams Center for Cosmology, Department of Physics, Carnegie Mellon University, Pittsburgh, PA 15213 USA

¹¹ Department of Physics, University of Arizona, 1118 E 4th St, Tucson, AZ 85721 USA

¹² SLAC National Accelerator Laboratory, Menlo Park, CA 94025 USA

¹³ Research Center for the Early Universe, University of Tokyo, 7-3-1 Hongo, Bunkyo-ku, Tokyo 113-0033, Japan

To be submitted to the Astrophysical Journal

ABSTRACT

We show that the projected number density profiles of SDSS photometric galaxies around galaxy clusters displays strong evidence for the splashback radius, a sharp halo edge corresponding to the location of the first orbital apocenter of satellite galaxies after their infall. We split the clusters into two subsamples with different mean projected radial distances of their members, $\langle R_{\text{mem}} \rangle$, at fixed richness and redshift, and show that the sample with smaller $\langle R_{\text{mem}} \rangle$ has a smaller ratio of the splashback radius to the traditional halo boundary $R_{200\text{m}}$, than the subsample with larger $\langle R_{\text{mem}} \rangle$, indicative of different mass accretion rates for the two subsamples. The same cluster samples were recently used by Miyatake et al. to show that their large-scale clustering differs despite their similar weak lensing masses, demonstrating strong evidence for halo assembly bias. We expand on this result by presenting a $6.6\text{-}\sigma$ detection of halo assembly bias using the cluster-photometric galaxy cross-correlations. Our measured splashback radii are smaller, while the strength of the assembly bias signal is stronger, than expectations from N-body simulations based on the Λ -dominated, cold dark matter structure formation model. Dynamical friction or cluster-finding systematics such as miscentering or projection effects are not likely to be the sole source of these discrepancies.

1. INTRODUCTION

Dark matter halos with masses larger than $10^{14} h^{-1} M_{\odot}$ collapse out of dense peaks in the primordial Gaussian density fluctuations that are believed to originate from quantum fluctuations in cosmic inflation (see e.g., Kaiser 1984; Bardeen et al. 1986, see Kravtsov & Borgani 2012 for a recent review). Clusters of galaxies form within such massive dark matter halos. The large scale clustering amplitude of the halos hosting galaxy clusters is thus heavily biased compared to the underlying matter distribution (Kaiser 1984; Mo & White 1996; Sheth et al. 2001; Tinker et al. 2010).

Although the large scale clustering amplitude of dark matter halos is primarily expected to depend upon the height of the initial density peak out of which a halo collapses (therefore its halo mass), it can have secondary dependencies on other parameters related to the assembly history of the halo, such as the radial profile of the initial peak, especially on cluster scales (Dalal et al. 2008). The dependence of the large scale clustering amplitude on parameters other than the halo mass has been broadly referred to as halo assembly bias, and has been studied in great detail using cosmological simulations (Sheth & Tormen 2004; Gao et al. 2005; Gao & White 2007; Wechsler et al. 2006; Li et al. 2008).

Halo assembly bias has however been difficult to establish in astrophysical observations. A clean detection of halo

assembly bias requires identifying samples of isolated halos which are matched in their halo masses but differ in their assembly histories. There have been several claims of detection of halo assembly bias on galaxy scales in the literature (e.g., Yang et al. 2006; Tinker et al. 2012; Hearin et al. 2014). However, Lin et al. (2015) investigated the first of these claims and found no strong evidence for halo assembly bias on galaxy scales. The difference in the conclusions was a result of contamination of the halo samples by satellite galaxies, or the differences in halo masses of the samples used to look for halo assembly bias (Lin et al. 2015).

Recently, Miyatake et al. (2015) presented the first evidence of halo assembly bias on cluster scales. Galaxy clusters offer two advantages: first, the probability of a cluster-sized halo being a satellite of an even bigger halo is much smaller than in the case of galaxies, and secondly, the weak gravitational lensing signal can be used to match galaxy cluster subsamples for their halo masses with a greater accuracy.

The galaxy cluster subsamples used by Miyatake et al. (2015) were drawn from the SDSS redMaPPer galaxy cluster catalog, and were matched in redshift and richness distribution, but differed in the compactness of the member galaxy distribution. These samples were shown to have very similar masses based on weak lensing, but had different large scale biases. The main goal of this paper is to observationally estab-

lish the connection between the member galaxy distribution and the mass assembly of these cluster subsamples without relying on proxies related to complicated baryonic physics, such as the star formation rates.

For this purpose, we use a unique probe of the mass assembly of galaxy clusters, which relies on the observational detection of the edges of galaxy clusters. Models of self-similar secondary infall of matter onto a spherical overdensity predict the presence of a density jump at the location where recently accreted material is reaching its first apocenter, associated with the last density caustic (Fillmore & Goldreich 1984; Bertschinger 1985). Although the collapse of matter onto realistic density peaks in cold dark matter models is considerably more complex than that envisioned in these models, the last density caustic manifests itself as a sharp steepening of the density profile in dark matter halos (Diemer & Kravtsov 2014).

The location of this density caustic, also called the splashback radius or the turnaround radius, can be used to define a physical boundary for dark matter halos (More et al. 2015). The splashback radius crucially depends upon the mass accretion rate of the collapsing halo (Vogelsberger et al. 2011; Diemer & Kravtsov 2014; Adhikari et al. 2014). For halos of the same mass, large accretion rate results in a smaller splashback radius. The physical reason is simple: the deeper the halo potential well gets during the orbit of a dark matter particle, the smaller is the value of its apocenter.

As discussed in More et al. (2015), hints for the splashback radius may have been seen before for individual clusters (Rines et al. 2013; Tully 2015; Patej & Loeb 2015). In this paper, we will harness the power of statistics to present the first high signal-to-noise detection of the splashback radius for our galaxy cluster subsamples. We will use the splashback radius to establish that these galaxy cluster subsamples have different mass accretion rates, and have different large scale clustering amplitude, a signature of halo assembly bias.

The paper is organized as follows:

- Section 2 describes the cluster subsamples and the Sloan Digital Sky Survey (SDSS) photometric galaxy data which form the basis of our study, and the methods we adopt in order to obtain the measurements of the galaxy number densities around our cluster subsamples.
- Section 3 presents our measurements of the galaxy number densities around our cluster subsamples, our inferences for the location of the splashback radius from these measurements, and our detection of halo assembly bias.
- Section 4 presents the predictions for the location of the splashback radius and the amount of halo assembly bias from numerical simulations in the context of the standard cosmological model. In particular, we discuss a number of systematic effects, which could affect our interpretation.
- The broad implications of our results are discussed in Section 5, and conclusions and a summary is presented in Section 6.

Throughout this paper, we adopt a flat Λ CDM cosmological model with matter density parameter $\Omega_m = 0.27$ and the Hubble parameter $h = 0.7$, unless otherwise stated. We use \log to denote logarithms with respect to base 10. We will use

r to denote three dimensional distances, and R for projected distances between galaxies or between galaxies and cluster centers. For cases where we want to preserve notations from previous papers, such as using R_{sp} for the splashback radius, we will specifically mention 2d or 3d to avoid confusion. The subscript 200m on halo mass M or radius R will refer to the mass or radius corresponding to spherical overdensity halos such that their boundaries enclose 200 times the mean matter density of the Universe.

2. DATA AND METHODS

We start from the publicly available catalog of galaxy clusters identified from the SDSS DR8 photometric galaxy catalog by the *red*-sequence *Matched-filter Probabilistic Percolation* (redMaPPer) cluster finding algorithm (v5.10, see the website¹ for details and Rykoff et al. 2014; Rozo et al. 2014). The cluster finder uses the *ugriz* magnitudes and their errors, to identify overdensities of red-sequence galaxies with similar colors as galaxy clusters. For each cluster, the catalog contains an optical richness estimate λ , a photometric redshift estimate z_λ , as well as the position and centering probabilities of 5 candidate central galaxies p_{cen} . A separate member galaxy catalog provides a list of members for each cluster, each of which is assigned a membership probability, p_{mem} .

The parent cluster catalog used in Miyatake et al. (2015) consists of an approximately volume limited sample of 8,648 redMaPPer clusters with $20 < \lambda < 100$ and $0.1 \leq z_\lambda \leq 0.33$. The average and the median redshift of our subsamples are 0.24 and 0.25, respectively. Throughout this paper we use the position of the most probable central galaxy in each cluster region as a proxy of the cluster center. However, we will discuss the effect of miscentering on our conclusions in Section 4.3.

In this paper, we subdivide this galaxy cluster sample into two subsamples following the same procedure as in Miyatake et al. (2015). Briefly, we obtain the average projected cluster-centric separation of member galaxies, $\langle R_{mem} \rangle$, for each cluster, and compute the median $\langle R_{mem} \rangle$ as a function of richness and redshift². We use this median to divide the parent sample into two subsamples. The large- and small- $\langle R_{mem} \rangle$ subsamples, labelled as low- and high- c_{gal} , respectively, in this paper, consist of 4,235 and 4,413 clusters, respectively.

In order to compute galaxy surface number density around these cluster subsamples, we make use of the photometric galaxy catalog from SDSS DR8 (Aihara et al. 2011). We exclude galaxies with any of the following flags: SATURATED, SATUR_CENTER, BRIGHT, DEBLENDED_AS_MOVING. We correct the magnitudes for galactic dust extinction using the maps of Schlegel et al. (1998), and use all photometric galaxies with extinction corrected *i*-band model magnitudes brighter than 21.0 and with magnitude errors less than 0.1.

We compute the stacked surface number density of the SDSS photometric galaxy samples around each of our cluster subsamples as a function of comoving projected separation, R , from the galaxy cluster center. Since our cluster subsamples span a wide range in redshift ($0.1 \leq z \leq 0.33$), the surface density profiles around lower redshift clusters will systematically contribute galaxies from a fainter photometric galaxy population. To avoid such biases, for our fiducial analysis, we only count cluster-galaxy pairs if the photometric galaxy has an absolute magnitude of $M_i - 5 \log h < -19.43^3$, assuming

¹ <http://risa.stanford.edu/redmapper/>

² While computing the average, we weight each galaxy's cluster centric distance with its membership probability (p_{mem}).

³ Note that we do not use any k-corrections or corrections for luminos-

that it is located at the redshift of the cluster (this limit corresponds to an apparent magnitude of $m_i = 21$ at $z = 0.33$ for our assumed cosmological model). Additionally, we will also present results for photometric galaxies that are one and two magnitudes brighter than our fiducial measurement, to explore the dependence of the splashback radius on the magnitude of photometric galaxies used.

We expect that the surface density measurement will consist of galaxies correlated with the galaxy clusters under consideration as well as uncorrelated galaxies in the foreground and the background. To determine this uncorrelated component, we compute the galaxy surface density around a sample of random points. We use 100 times larger number of random points than the number of clusters in our subsamples⁴. These random points incorporate the survey geometry, depth variations, and distributions of clusters in redshift and richness. We subtract the background around random points from the total to obtain the surface density of correlated galaxies, $\Sigma_g(R)$. We use 102 jackknife regions in order to compute the covariance in the measurements of $\Sigma_g(R)$ with typical size of 10×10 sq. deg. which corresponds to about $100 \times 100 (h^{-1}\text{Mpc})^2$ at the median redshift of our cluster subsamples. The jackknife regions are thus significantly larger compared to the scales of interest in this paper, justifying the assumptions behind the jackknife errors.

Using the measurement of the galaxy surface densities, we would like to infer the location of the splashback radius of our cluster subsamples, i.e., the steepest logarithmic slope of the galaxy number density distributions in three dimensions. Given that the splashback radius is expected to be of the order of R_{200m} of our halos, we fit the surface densities in the range $[0.1, 5.0] h^{-1}\text{Mpc}$. The location of the steepening in three dimensions is expected to be different from that in projection (Diemer & Kravtsov 2014). Therefore, we will use a 3-dimensional parameterization first proposed by Diemer & Kravtsov (2014) to forward model the projected measurements (see also More et al. 2015). The model consists of inner and outer surface density profiles with a smooth transition between the two,

$$\begin{aligned} \rho_g(r) &= \rho_g^{\text{inner}} f_{\text{trans}} + \rho_g^{\text{outer}}, \\ \rho_g^{\text{inner}} &= \rho_s \exp\left(-\frac{2}{\alpha} \left[\left(\frac{r}{r_s}\right)^\alpha - 1\right]\right), \\ \rho_g^{\text{outer}} &= \rho_o \left(\frac{r}{r_{\text{out}}}\right)^{-s_c}, \\ f_{\text{trans}} &= \left[1 + (r/r_t)^\beta\right]^{-\gamma/\beta}, \\ \Sigma_g(R) &= 2 \int_0^{z_{\text{max}}} \rho_g\left(\sqrt{R^2 + z^2}\right) dz. \end{aligned} \quad (1)$$

Note that the above fitting formula, which is an Einasto profile in the inner regions which transitions to a power law in the outer regions, is able to reproduce the dark matter profile around halos, and is flexible enough to reproduce the simulation results compared to other fitting formulae such as the Navarro-Frenk-White model and the halo model (Navarro et al. 1996; Oguri & Hamana 2011; Hikage et al. 2013). Here we simply assume that the same fitting formula is also flexi-

ble enough to reproduce the galaxy surface density measured from the SDSS data.⁵ We chose the maximum projection length $z_{\text{max}} = 40 h^{-1}\text{Mpc}$ as our default value, and we have checked that the location of the splashback radius is insensitive to this choice, in particular reducing z_{max} to be even as small as $10 h^{-1}\text{Mpc}$.

ble enough to reproduce the galaxy surface density measured from the SDSS data.⁵ We chose the maximum projection length $z_{\text{max}} = 40 h^{-1}\text{Mpc}$ as our default value, and we have checked that the location of the splashback radius is insensitive to this choice, in particular reducing z_{max} to be even as small as $10 h^{-1}\text{Mpc}$.

Given that the parameter r_{out} and ρ_o are entirely degenerate with each other, we fix $r_{\text{out}} = 1.5 h^{-1}\text{Mpc}$. We find that allowing α to vary freely results in an almost perfect degeneracy between ρ_s and r_s , with very little impact on the location of the steepening of the galaxy density profiles. Therefore we use a prior on $\log \alpha = \log 0.2 \pm 0.6$, centered at the value expected for the dark matter halos corresponding to our mass estimates from weak lensing (Gao et al. 2008). For our fiducial modeling scheme, we also use priors on $\log \beta = \log 4.0 \pm 0.2$ and $\log \gamma = \log 6.0 \pm 0.2$ centered around the values recommended by Diemer & Kravtsov (2014) and constrain the parameters r_s and r_t to lie within $[0.1, 5.0] h^{-1}\text{Mpc}$.

For our default modeling scheme, we assume that the most probable central galaxy for every cluster (one with the highest p_{cen}), assigned in the redMaPPer catalog, resides at the true center of gravitational potential in each cluster region. However, as studied in Miyatake et al. (2015) (see also Hikage et al. 2013), some fraction of the central galaxies in our cluster subsamples may be mis-centered, characterized by offset radii ranging from $400 h^{-1}\text{kpc}$ possibly up to $800 h^{-1}\text{kpc}$. If such mis-centered clusters are indeed present in large numbers, our measurements of the splashback radius would be biased high. We will present tests for the effects of mis-centering in Section 4.3 below.

We will use the affine invariant Markov Chain Monte Carlo sampler of Goodman & Weare (2010), as implemented in the software package *emcee* (Foreman-Mackey et al. 2013), in order to sample from the posterior distribution of the parameters, $\log \rho_s$, $\log r_s$, $\log \alpha$, $\log r_t$, $\log \gamma$, $\log \beta$, $\log \rho_o$ and s_c , given the galaxy surface density measurements and the stated priors.

As a test of our fitting method, in Appendix A we apply it to projected number density distributions of (sub)-halos around galaxy clusters in numerical simulations (see below for the details of the simulations) and show that we are able to recover the location of the steepening of the three dimensional density distribution of subhalos quite accurately with our modelling scheme.

3. RESULTS

3.1. Splashback in galaxy number density profiles

We begin by presenting how the stacked surface density profile of galaxies, $\Sigma_g(R)$, around the entire parent sample of redMaPPer clusters, described in the previous section, varies with galaxy samples of different absolute magnitude thresholds. These measurements are shown in the top panels of Figure 1 using points with errorbars. The brightness of the photometric galaxy sample increases from left to right. The solid lines in the bottom panels correspond to the profiles of the logarithmic slope of the galaxy surface densities. These slope profiles were obtained by using the Savitzky-Golay algorithm to smooth the observed measurements, by fitting a third-order polynomial over a window of five neighbouring points, and then using a cubic spline to interpolate between

⁴ We have tested that the use of the improved random catalog from Rykoff et al. (2016) does not change any conclusions in this paper.

⁵ Tests using subhalo density profiles around cluster scale halos from simulations presented in Appendix A, as well as the reasonable values of χ^2 values we obtain for describing the observed measurements justify this choice.

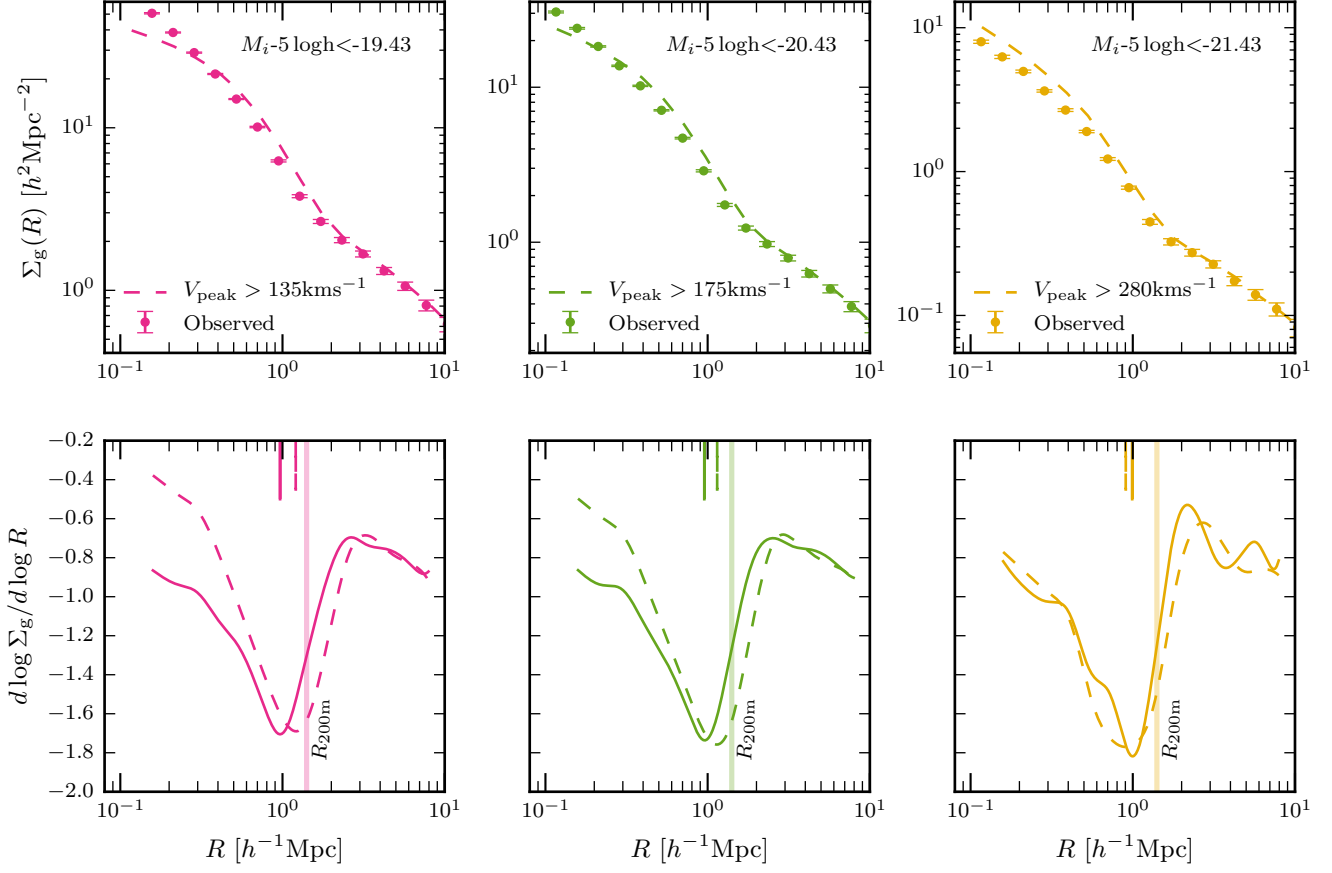


Figure 1. *Top panels:* The surface number density profiles, $\Sigma_g(R)$, of SDSS photometric galaxies with different magnitude thresholds around the entire redMaP-Per cluster sample with $z \in [0.1, 0.33]$ and richness $\lambda \in [20, 100]$, are shown using symbols with errorbars. The dashed lines correspond to (sub)-halo surface density profiles in the Multidark Planck II simulation around clusters with the mass threshold similar to our sample at $z = 0.248$. The threshold on subhalo V_{peak} values roughly correspond to the magnitude thresholds in each panel and were obtained by subhalo abundance matching (see Appendix B). *Bottom panels:* The logarithmic slope of the surface density profiles are shown using solid and dashed lines for the observed galaxy and the subhalo surface density profiles, respectively. The observed slope of the surface density profile has a shape which is similar to that expected from simulations. Note that although the surface density profiles both in observations and simulations exhibit similar steepening, the corresponding radii of the steepest slope are at slightly different locations.

Table 1
Posterior distribution of parameters from the MCMC analysis

Magnitude	c_{gal}	$\log \rho_0$	$\log \alpha$	$\log r_s$	$\log \rho_o$	s_e	$\log r_t$	$\log \beta$	$\log \gamma$	R_{sp}^{2d}	R_{sp}^{3d}	χ^2/dof
-19.43	high	$1.10^{+0.25}_{-0.77}$	$-0.95^{+0.22}_{-0.32}$	$-0.32^{+0.40}_{-0.13}$	$0.349^{+0.031}_{-0.035}$	$1.601^{+0.076}_{-0.080}$	$-0.082^{+0.049}_{-0.040}$	$0.762^{+0.119}_{-0.095}$	$0.66^{+0.14}_{-0.12}$	$0.778^{+0.015}_{-0.014}$	$0.971^{+0.025}_{-0.021}$	6.0/8
-19.43	low	$-0.68^{+0.30}_{-0.20}$	$-1.090^{+0.088}_{-0.063}$	$0.55^{+0.11}_{-0.17}$	$0.545^{+0.055}_{-0.067}$	$1.600^{+0.068}_{-0.080}$	$0.058^{+0.023}_{-0.021}$	$1.10^{+0.12}_{-0.11}$	$0.64^{+0.13}_{-0.11}$	$1.153^{+0.029}_{-0.021}$	$1.378^{+0.026}_{-0.026}$	13.2/8
-20.43	high	$0.70^{+0.31}_{-0.86}$	$-0.97^{+0.28}_{-0.35}$	$-0.27^{+0.45}_{-0.16}$	$0.167^{+0.014}_{-0.018}$	$1.613^{+0.074}_{-0.077}$	$-0.098^{+0.048}_{-0.038}$	$0.82^{+0.13}_{-0.12}$	$0.69^{+0.14}_{-0.12}$	$0.756^{+0.014}_{-0.012}$	$0.938^{+0.024}_{-0.025}$	2.9/8
-20.43	low	$-0.89^{+0.38}_{-0.28}$	$-1.019^{+0.118}_{-0.086}$	$0.48^{+0.15}_{-0.21}$	$0.276^{+0.018}_{-0.021}$	$1.655^{+0.052}_{-0.056}$	$0.072^{+0.026}_{-0.023}$	$1.10^{+0.12}_{-0.11}$	$0.80^{+0.14}_{-0.13}$	$1.128^{+0.025}_{-0.024}$	$1.352^{+0.028}_{-0.025}$	12.4/8
-21.43	high	$0.10^{+0.39}_{-0.93}$	$-1.00^{+0.33}_{-0.35}$	$-0.25^{+0.49}_{-0.20}$	$0.0385^{+0.0045}_{-0.0048}$	$1.496^{+0.096}_{-0.099}$	$-0.087^{+0.051}_{-0.044}$	$0.85^{+0.14}_{-0.12}$	$0.78^{+0.15}_{-0.13}$	$0.754^{+0.022}_{-0.019}$	$0.938^{+0.036}_{-0.040}$	10.5/8
-21.43	low	$-1.31^{+0.45}_{-0.37}$	$-0.97^{+0.16}_{-0.12}$	$0.40^{+0.20}_{-0.25}$	$0.0712^{+0.0063}_{-0.0066}$	$1.624^{+0.073}_{-0.073}$	$0.087^{+0.026}_{-0.025}$	$1.12^{+0.14}_{-0.13}$	$0.90^{+0.15}_{-0.14}$	$1.132^{+0.043}_{-0.035}$	$1.361^{+0.034}_{-0.038}$	23.6/8

Note. — The different rows list the 68% confidence intervals on the model parameters (see Eq. 1) given the surface number density data shown in Figure 2. The χ^2 per degree of freedom as well as the inferred 2-d and 3-d splashback radius are also shown in the last three columns.

these smoothed measurements. In contrast with the traditional Savitzky-Golay algorithm, we explicitly account for the covariant errors on these data points, as proposed by More (2016a)⁶.

In Appendix B, we have used subhalo abundance matching to obtain an estimate of the approximate V_{peak} (the maximum circular velocity of a halo throughout its entire history) value of dark matter subhalos⁷ hosting our photometric galaxies as a function of their magnitude. To compare the

observed surface density profiles with those expected from the standard structure formation model, we utilize Multidark Planck II (MDPL2), a 3840^3 particle cosmological N-body simulation with box size of $1h^{-1}\text{Gpc}$ and mass resolution of $1.51 \times 10^9 h^{-1} M_{\odot}$ (Klypin et al. 2014). We also use the associated halo catalogs found using Rockstar, a halo finder which groups particles into halos using their phase space information (Behroozi et al. 2013)⁸.

as well, not just satellite halos. We will use the term halos explicitly when referring to only isolated halos.

⁸ These catalogs are publicly available at the website <http://www.>

⁶ https://github.com/surhudm/savitzky_golay_with_errors

⁷ Our use of the term subhalos henceforth includes isolated host halos

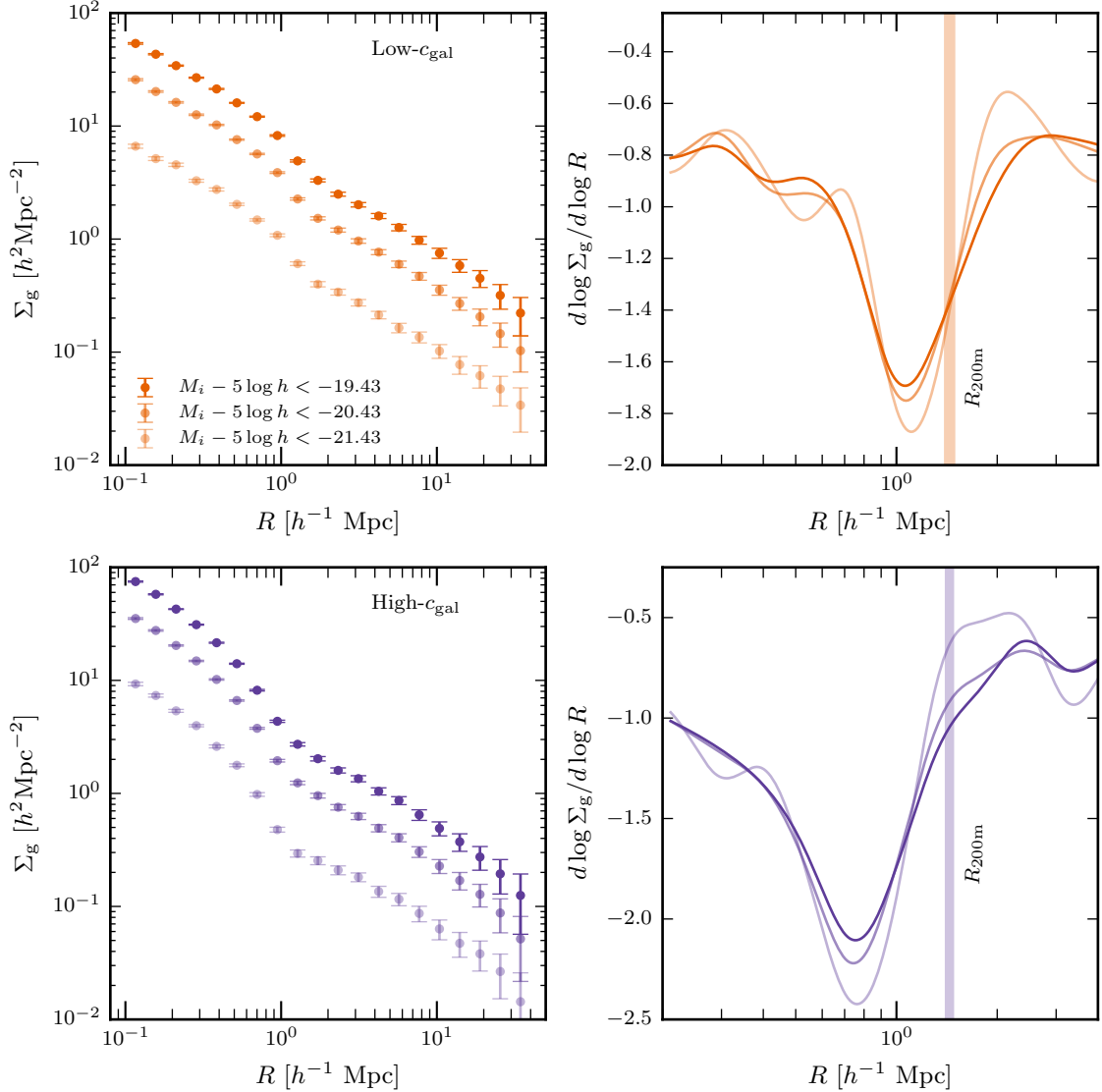


Figure 2. *Left panels:* The surface number density profiles, $\Sigma_g(R)$, of SDSS photometric galaxies around the low- c_{gal} (top) and high- c_{gal} (bottom) cluster subsamples. The three different point types with errorbars in each panel correspond to the three different magnitude limited samples of photometric galaxies we use. *Right panels:* The logarithmic density slope of the surface number density profiles obtained after smoothing the data points with an improved Savitzky-Golay filter (order 3, window size 5). The two-dimensional splashback radius corresponds to the location of the steepest slope or the minimum of $d \log \Sigma_g / d \log R$. For comparison, the shaded regions correspond to the traditional halo boundary, $R_{200\text{m}}$, estimated using the posterior distribution of halo masses from the weak lensing profile for each cluster subsample from Miyatake et al. (2015) (both are consistent with each other within the errorbars). Note that the steepest slope (i.e., the minimum in $d \log \Sigma_g / d \log R$) occurs at different locations for the two cluster subsamples.

The dashed lines in the top and bottom panels of Figure 1 correspond to the expected subhalo surface density profiles around clusters in the cosmological simulation Multidark Planck II at $z = 0.248$. We have selected cluster sized halos above a mass threshold of $10^{14} h^{-1} M_{\odot}$, which results in the same average halo mass as that of our sample. We have normalized the surface density profiles in the top panels to match the observations at $\sim 11 h^{-1} \text{Mpc}$. There are marked similarities between the density profiles of subhalos in simulations and the galaxies in observations. The surface number densities strongly deviate from a simple power law and show a clear break on scales of $\sim 1 h^{-1} \text{Mpc}$ in both observations and simulations. This is most clearly seen in the bottom panels, where we see that the profiles reach their steepest slope on scales of $\sim 1 h^{-1} \text{Mpc}$. This steepening, associated with the

splashback radius, is also seen in observations, as expected from subhalo surface density profiles in simulations. However, it is also clear that the locations where the surface density profiles reach their steepest slopes are different between observations and simulations, especially for the left and the middle panels. This discrepancy between the observed and expected splashback radii is also seen for the cluster subsamples, which we investigate at length next. We will extensively quantify, comment and explore this discrepancy in the location of splashback radius around these cluster subsamples.

The surface density of photometric galaxies around the low- and high- c_{gal} cluster subsamples are shown in the upper and lower panels of Figure 2 using orange and purple symbols with errorbars, respectively. The lighter shades correspond to photometric galaxies with brighter magnitude limits. The solid lines in the upper and lower right hand panels of Fig-

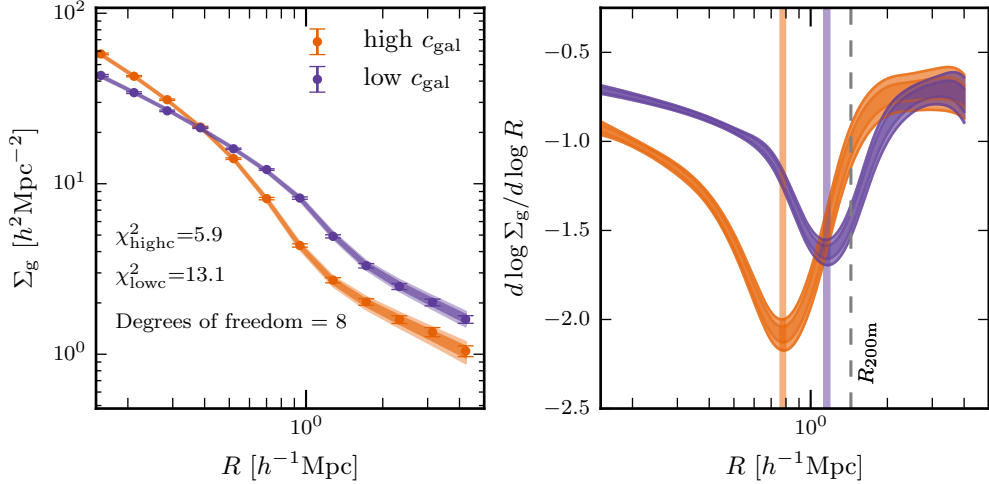


Figure 3. The surface number density profiles, $\Sigma_g(R)$, of our fiducial sample of SDSS photometric galaxies around the two cluster subsamples are shown in the left hand panel. The shaded regions show the 68 and 95 percent confidence regions of our model fit to the data. The right hand panel shows the inferred constraints on the logarithmic slope of $\Sigma_g(R)$ for the two subsamples. The splashback radius in 2d, $R_{\text{sp}}^{2\text{d}}$, corresponds to the location of the steepest slope or the minimum of $d \log \Sigma_g / d \log R$. The 68 percent constraints on $R_{\text{sp}}^{2\text{d}}$ are marked with vertical shaded regions. These minima occur at significantly different locations for the two cluster subsamples. The traditional halo boundary, $R_{200\text{m}}$, is marked by the grey dotted vertical line.

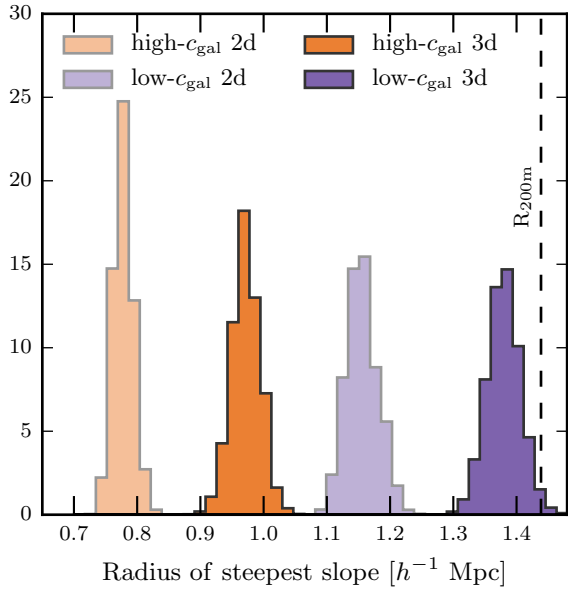


Figure 4. The posterior distributions for the location of the steepest slope of the galaxy density profiles around the high- and low- c_{gal} cluster subsamples are shown in orange and purple colored histograms, respectively. The light shaded histograms correspond to the location of the steepest slopes of the surface density profiles (2-d), while the dark shaded histograms correspond to the location of steepest slope of the 3-d number density profiles inferred by our fits. The locations of the steepest slopes for the two cluster subsamples are significantly different, implying a different mass accretion rate onto these cluster subsamples.

ure 2 show the logarithmic slope of the surface density profiles around the two subsamples. The slopes for both cluster subsamples reach values steeper than ~ -1.6 on either side of $\sim 1 h^{-1}\text{Mpc}$. The surface density of galaxies around the high- c_{gal} cluster subsample reaches its steepest slope at a smaller radius compared to the low- c_{gal} subsample. The value of the steepest slope is considerably larger for the high- c_{gal} cluster subsample than the low- c_{gal} subsample. A comparison between the profiles of galaxies as a function of different magnitude thresholds around any given cluster subsamples shows

very little difference in the location of the steepest slope in projection.

We fit the galaxy surface density profiles with the model described in the previous section. The median and the 68 percent confidence intervals of the posteriors of each of these parameters, as well as the best fit χ^2 values are listed in Table 1. The number of degrees of freedom for our model is 8.

We show the 68 and 95 percent confidence regions from the fits to the surface density of the fiducial sample of photometric galaxies around both our cluster subsamples in the left hand panel of Figure 3. The corresponding confidence regions for the logarithmic slope, including marginalization over other model parameters, are shown in the right hand panel. We use the samples from the posterior of the model parameter space to infer the location of the steepest slope of the projected galaxy density profile, $R_{\text{sp}}^{2\text{d}}$, and its uncertainty. These numbers are reported for all of our subsamples and for the different models in Table 1 as well.

The location of the splashback radius can be compared with the traditional halo boundary definition, $R_{200\text{m}}$ for each subsample. This is shown by the vertical shaded bands in the right panels of Figure 2, as estimated from the posterior distribution of the halo masses for our two subsamples inferred from the weak lensing measurement in Miyatake et al. (2015).

We now use the samples from the posterior distribution of model parameters to infer the constraints on the location of the minimum of the logarithmic derivative of the three dimensional galaxy density profile, $d \log \rho_g / d \log r$. The resultant constraints on $R_{\text{sp}}^{3\text{d}}$ are reported in the penultimate column of Table 1. The inferred value of $R_{\text{sp}}^{3\text{d}}$ is always larger than the corresponding $R_{\text{sp}}^{2\text{d}}$ for all photometric galaxy samples around both cluster subsamples, as shown explicitly in Figure 4. The vertical dashed line corresponds to the traditional halo boundary definition, $R_{200\text{m}}$, for the two subsamples.

Note that, for our model, a transition function $f_{\text{trans}} = 1$, would correspond to a simple density profile: a sum of Einasto profile which describes well the inner regions and a power law profile for the outer regions. However, the data strongly disfavor such a model, with χ^2 values ranging from

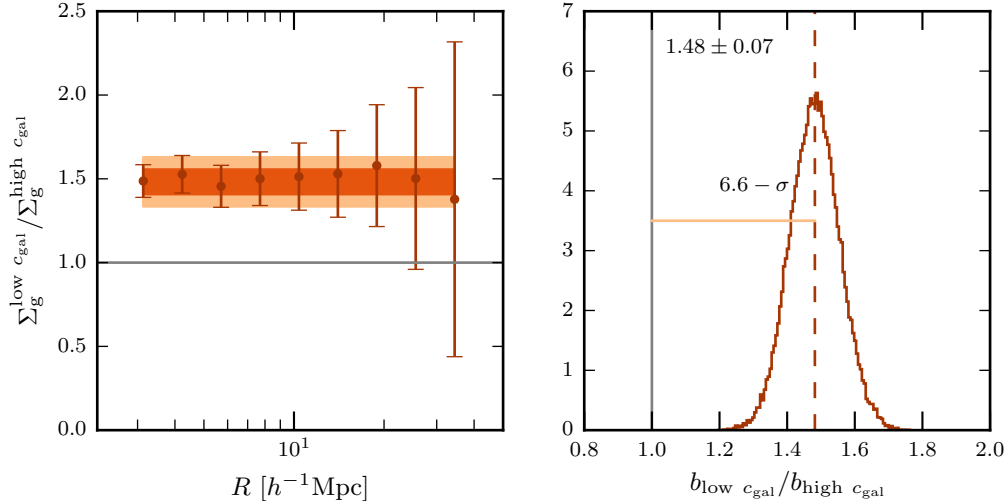


Figure 5. Detection of the halo assembly bias. *Left panel:* The ratio of the surface number density profiles of our fiducial samples of photometric galaxies around the two galaxy cluster subsamples. The shaded regions correspond to the 1- and 2-sigma confidence regions for a single constant parameter fit to these data. *Right panel:* The posterior distribution of the ratio given the measurements shown in the left panel. We detect the assembly bias – difference in the halo biases of the two samples – at 6.6σ . There is a significant covariance in the errors, hence the small point-to-point variation given the errors. The quoted significance accounts for the covariance.

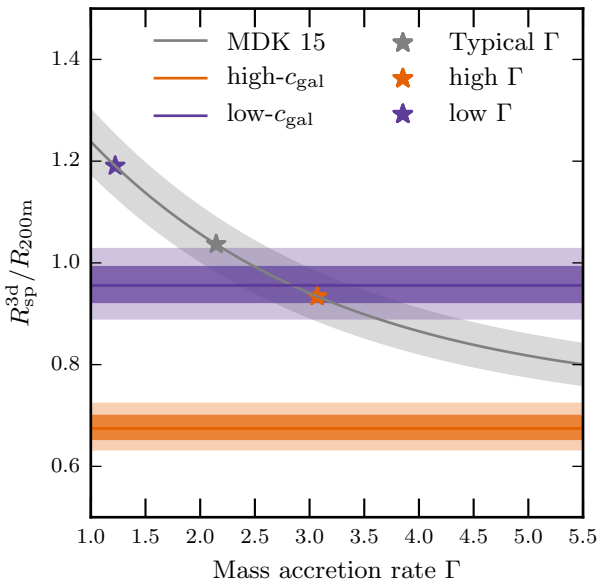


Figure 6. The dependence of $R_{\text{sp}}/R_{200\text{m}}$ on the accretion rate Γ at $z = 0.24$ predicted by Λ CDM, shown by a gray line with 5% uncertainty (More et al. 2015). The dark and faint shaded purple (orange) regions display the 68 and 95 percent confidence limits on the splashback radius in 3d for our low- (high-) c_{gal} sample. The gray, orange and purple stars correspond to the typical splashback radii for a typical accretion rate, as well as slow and fast accreting clusters from numerical simulations (see text for details). The observed values of the splashback radii are significantly smaller than the predicted values their halo masses, even if we consider halos with typical accretion rates.

60 to 140 for 9 degrees of freedom depending upon the cluster subsample and the photometric galaxies under consideration⁹. Therefore, *our measurements imply a steepening of the number density profile of galaxies around both of our cluster subsamples beyond that predicted by the Einasto profile.*

⁹ There is only 1 additional degree of freedom for these models, as we lose only one free parameter r_1 , the other parameters γ and β have priors in the fiducial modeling scheme and thus do not change the degrees of freedom.

3.2. Detection of Halo Assembly bias

The mean number density profile of galaxies correlated with clusters at large separations is proportional to the product of the biases of clusters and galaxies in the photometric sample. We have shown above that these profiles are different for the low- and high- c_{gal} cluster subsamples. Given that our cluster samples have the same redshift distribution, the bias of photometric galaxies should cancel out in the ratio of the number density profiles, and we can use the ratio to test whether the two cluster subsamples have different intrinsic clustering biases, as recently reported by Miyatake et al. (2015).

In the left hand panel of Figure 5, we show the ratio of the number density profiles for our fiducial sample of photometric galaxies around the two subsamples of galaxy clusters on scales of $3 - 40 h^{-1}$ Mpc. We fit a constant ratio to these measurements accounting for the covariance determined from the jackknife technique. This assumes that the two samples have similar scale dependence for their bias, and the data support this assumption. The posterior distribution of the constant ratio obtained using this procedure is shown in the right hand panel of Figure 5. We find a 6.6σ deviation of the ratio of the two surface density profiles from unity: 1.48 ± 0.07 . We have thus detected halo assembly bias – the two cluster subsamples have the same halo mass based on weak lensing, but a different large scale halo bias. For comparison, the difference in the bias ratio that was obtained in Miyatake et al. (2015) using the weak lensing signal was $1.64^{+0.31}_{-0.26}$, and that from the auto-correlation function of galaxy clusters was 1.40 ± 0.09 . The three different measurements give results which are statistically consistent with each other.

4. COMPARISONS WITH EXPECTATIONS FROM Λ CDM MODEL

Using the projected galaxy number density profiles around two cluster subsamples from the redMaPPer catalog, we have shown that these two subsamples have different profiles, splashback radii, as well as a different clustering bias. We now compare these measurements to the predictions of the concordance cosmological Λ CDM model.

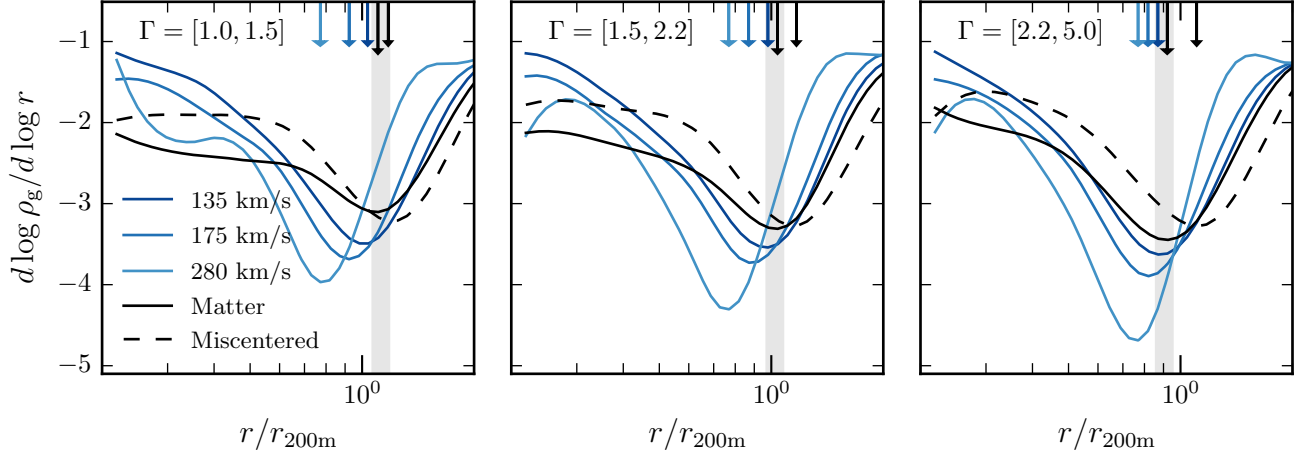


Figure 7. Comparison between the logarithmic slope of the density profile for matter and that of subhalos selected using different V_{peak} thresholds as indicated in the legend. Different panels correspond to halos with different mass accretion rates, Γ . The arrows indicate the location of the steepest slope, or the splashback radii for the corresponding population, with the longest arrow used to represent dark matter. The grey vertical bands corresponds to the fitting function for $R_{\text{sp}}/R_{200\text{m}}$ similar to the one by More et al. (2015), but for the mean profiles, and includes an uncertainty of $\pm 5\%$.

4.1. Is the splashback radius for the two subsamples at the expected location?

Using the weak lensing inferred masses for our cluster subsamples, we can compute the baseline expectation for the location of the splashback radius in the standard cosmological model. The ratio $R_{\text{sp}}^{\text{3d}}/R_{200\text{m}}$ is expected to depend upon the accretion rate of the halos as well as redshift (Diemer & Kravtsov 2014; Adhikari et al. 2014; More et al. 2015). To compute the mean accretion rate on to halos, we use halos from MDPL2 at $z = 0.248$, closest to the median redshift of our redMaPPer subsamples and select all halos above a certain halo mass threshold¹⁰. We choose the halo mass threshold such that the average halo mass of the sample is consistent with the $M_{200\text{m}}$ of the redMaPPer subsamples obtained by Miyatake et al. (2015). As a best case expectation, we divide the halo sample into two based on the dependence of the halo mass accretion rate on halo mass, $\Gamma(M_{200\text{m}}) = \Delta \log M_{\text{vir}}/\Delta \log a$. The derivative for Γ is computed using a finite difference scheme using the virial masses at redshift 0.248 and 0.748 (Diemer & Kravtsov 2014; More et al. 2015)¹¹.

In Figure 6, we compare the location of the splashback radius with respect to $R_{200\text{m}}$ observed for our cluster subsamples, to the best case expectations implied by these accretion rates. The grey band corresponds to the fitting function

$$\frac{R_{\text{sp}}^{\text{3d}}}{R_{200\text{m}}} = 0.58 [1 + 0.63 \Omega_m(z)] \left(1 + 1.08 \exp \left[-\frac{\Gamma}{2.26} \right] \right) \quad (2)$$

with a 5 percent uncertainty. This fitting function is a good fit to the splashback radii of dark matter halos in simulations used in More et al. (2015)¹², but corresponds to the mean profiles instead of the median. The grey star corresponds to the typical expected value of Γ for halos in the sample, estimated from the simulations, while the orange and purple stars similarly correspond to the average Γ for the best-case simulation subsamples with the fastest and slowest ac-

cretion rates (see above). The data seem to prefer a much smaller splashback radius for each of our cluster subsamples ($R_{\text{sp}}^{\text{3d}}/R_{200\text{m}} = 0.675^{+0.024}_{-0.021}$ and 0.955 ± 0.035 for the high- and the low- c_{gal} subsamples, respectively), even when compared to the splashback radius corresponding to halos with typical Γ for our mass scales.

4.2. Does dynamical friction result in a smaller splashback radius?

So far in our analysis, we have identified the splashback radius using the galaxy distribution around our cluster subsamples. The splashback radius of galaxies could be different from that of dark matter due to dynamical friction acting on the subhalos that host our galaxies, provided these subhalos are sufficiently massive (Adhikari & Dalal 2016). In what follows, we show that the steepening of the three dimensional density profiles for both matter and subhalos that host our fiducial photometric sample of galaxies are expected to occur at similar locations.

For this purpose, we again make use of the halo and subhalo catalogs from the MDPL2 simulation. We match the cumulative abundances of dark matter subhalos as a function of V_{peak} (the maximum circular velocity of a halo throughout its entire history) and that of our photometric galaxies as a function of their magnitude, to obtain an estimate of the V_{peak} of subhalos hosting our galaxies (see Appendix B). The subhalos that host our fiducial subsample of photometric galaxies approximately correspond to subhalos with $V_{\text{peak}} > 135 \text{ km s}^{-1}$, while the brighter subsamples correspond to subhalos with $V_{\text{peak}} > 175 \text{ km s}^{-1}$ and $V_{\text{peak}} > 280 \text{ km s}^{-1}$, respectively.

For this analysis, we use the $z = 0$ particle snapshot of the simulation¹³. We use all halos identified by the 6d phase space halo finder ROCKSTAR (Behroozi et al. 2013) in the $z = 0$ snapshot with halo mass, $M_{200\text{m}}$, above $8.5 \times 10^{13} h^{-1} M_{\odot}$ as our sample of galaxy clusters. We subdivide these in bins of $\Gamma = \Delta \log M_{\text{vir}}/\Delta \log a$, and compute the three-dimensional density profile of matter around them. The derivative for Γ for this particular snapshot was computed between $z = 0$ and $z = 0.5$ (Diemer & Kravtsov 2014; More et al. 2015). The log-

¹⁰ Using a cosmological simulation with $\Omega_m = 0.27$, we get similar numbers for the expected mass accretion rates.

¹¹ There is very little difference in the average value of Γ if we use a halo mass sample with a threshold on N_{sat} .

¹² The fitting function was calibrated in the redshift range [0, 4].

¹³ Ideally we would have liked to also carry out this exercise near $z = 0.24$, but we had only the $z = 0$ particle snapshot available.

arithmic slope of the matter density profile around the cluster samples are shown in the different panels of Figure 7 using a black solid line. For reference we also show the expected locations of the splashback radius for each of the subsamples, using Equation 2. The fitting function seems to capture the trend observed for the splashback radius of dark matter as a function of the accretion rate in the simulation reasonably well (within 5 percent).

In the same figures we also show the logarithmic slopes of subhalo distributions around galaxy cluster halos for different V_{peak} thresholds obtained from our simple subhalo abundance matching method. We observe that the locations of the steepest slope for subhalos with the lowest V_{peak} threshold is similar to that in dark matter within 5 percent for all the Γ bins shown in the figure. Thus the location of the splashback radius is not expected to be significantly different for subhalos hosting our fiducial sample of photometric galaxies. As we consider V_{peak} thresholds corresponding to our brighter subsamples, we see effects of dynamical friction acting on the subhalos (see also Jiang & van den Bosch 2014). The splashback radius of these larger subhalos systematically shifts to smaller values with increasing V_{peak} threshold.

We have tried to maximise the effect of dynamical friction in the above exercise by not considering scatter between the luminosity of galaxies and the V_{peak} of their subhalos while performing abundance matching. We do not see a large shift in the splashback radius of the photometric galaxies around any of our cluster subsamples as a function of their magnitude threshold. However, this does not imply that our data rule out dynamical friction acting on the brighter sample of photometric galaxies. It is quite likely that there is a reasonably large scatter between the magnitude and V_{peak} , which can wash out the dynamical friction effect.

4.3. Background subtraction and mis-centering uncertainties

We have used the number density profiles around random points to subtract the uncorrelated galaxies in the background and the foreground of our subsamples. We have also tested how residual uncertainties in background subtraction can affect our results. As an initial test of uncertainties in the background which are constant with radius, we have added in a constant parameter to our model for the projected number density profiles. Even after marginalizing over such a parameter, we obtain values for the splashback radii and its uncertainty which are very consistent in two dimensions, and virtually identical in three dimensions. However, there could be additional background uncertainties which vary with the projected distance.

For example, we expect that the clusters in our subsamples will cause the galaxies in the background to be magnified (see e.g., Umetsu et al. 2011). We explore the changes to the background due to cluster magnification in Appendix D, and find that the splashback radius is not affected even after applying a conservative correction to the background due to the magnification of the clusters. The sky subtraction around bright or highly clustered objects can also potentially affect the photometry of galaxies and hence the background objects in clusters (Aihara et al. 2011). This can also partly cancel the magnification effect, as it reduces the number density of background galaxies in clusters.

Mis-centering of central galaxies in redMaPPer clusters could affect the profiles and our estimates of the splashback radius. There are two kinds of mis-centering: first, a galaxy may be mis-classified as a central by the cluster finder and

second, the central galaxy may be physically displaced from the potential minimum of the cluster around which all galaxies orbit. To test for the first kind of mis-centering, we have restricted our model fits to scales $> 400 h^{-1} \text{kpc}$ or to using clusters where the most probable central galaxy has $p_{\text{cen}} > 0.9$. These restrictions produce fit parameters consistent with those listed in Table 1, especially the position of the splashback radius, within the reported uncertainties.

To test for the second kind of mis-centering, we have also considered all halos from the MDLP2 simulation used in the previous section, and displaced 40 percent of these halos in their positions with an offset drawn from a multivariate Gaussian distribution with standard deviation equal to $400 h^{-1} \text{kpc}$ ¹⁴. In each panel of Figure 7, we have additionally included a dashed line which shows the slope of the logarithmic density profiles around such a sample of halos. We find that, as expected, in all cases the splashback radius would be overestimated by $\gtrsim 20\%$, an effect which goes in the opposite direction required to explain a smaller splashback radius. Moreover, the change of slope around the splashback radius is much less pronounced and overall shape of the profile is significantly modified. This is in contrast with the good agreement we find between the *shapes* of the predicted and observed slope profiles.

4.4. Could averaging effects result in a smaller splashback radius?

We have used the average halo mass of our subsamples as inferred from weak lensing to obtain the average $R_{200\text{m}}$ of our cluster halos to compare with the observed values of the splashback radius, $R_{\text{sp}}^{3\text{d}}$. Could the difference between the $R_{\text{sp}}^{3\text{d}}/R_{200\text{m}}$ seen in observations and that predicted from simulations arise due to the finite width of the halo mass distribution? We considered the distribution of halo masses resulting from a threshold sample with the same average halo mass as our cluster subsamples. For such samples, we find that the difference between $\langle R_{200\text{m}} \rangle$ and that inferred from the average halo mass is different by only ≈ 3 percent, whereas the discrepancy we observe is much larger¹⁵.

We have also verified that the location of the splashback radius for a threshold mass sample does not result in a smaller inferred splashback radius compared to the expectation based on using the average halo mass, and the average mass accretion rate onto the halo samples. These tests confirm that the smaller value for the splashback radius we observe is not likely to be a result of some averaging effects.

4.5. What is the systematic error in the weak lensing halo masses?

Our conclusion that the observed splashback radius is smaller than the expectation from simulations is based on the comparison with the virial radius for weak lensing halo mass inferred by Miyatake et al. (2015). However, Miyatake et al. (2015) assumed a δ -function distribution in halo masses to model the weak lensing measurements for each cluster subsample and infer the average halo mass. Such a simplified

¹⁴ This assumes that the redMaPPer centering probabilities are unreliable and the centering algorithm performs as badly as selecting the brightest galaxy in the cluster, which could result in 40 percent mis-centering fraction (Skibba et al. 2011).

¹⁵ Using a halo mass sample with a threshold in N_{sat} as in our data, also does not affect this conclusion.

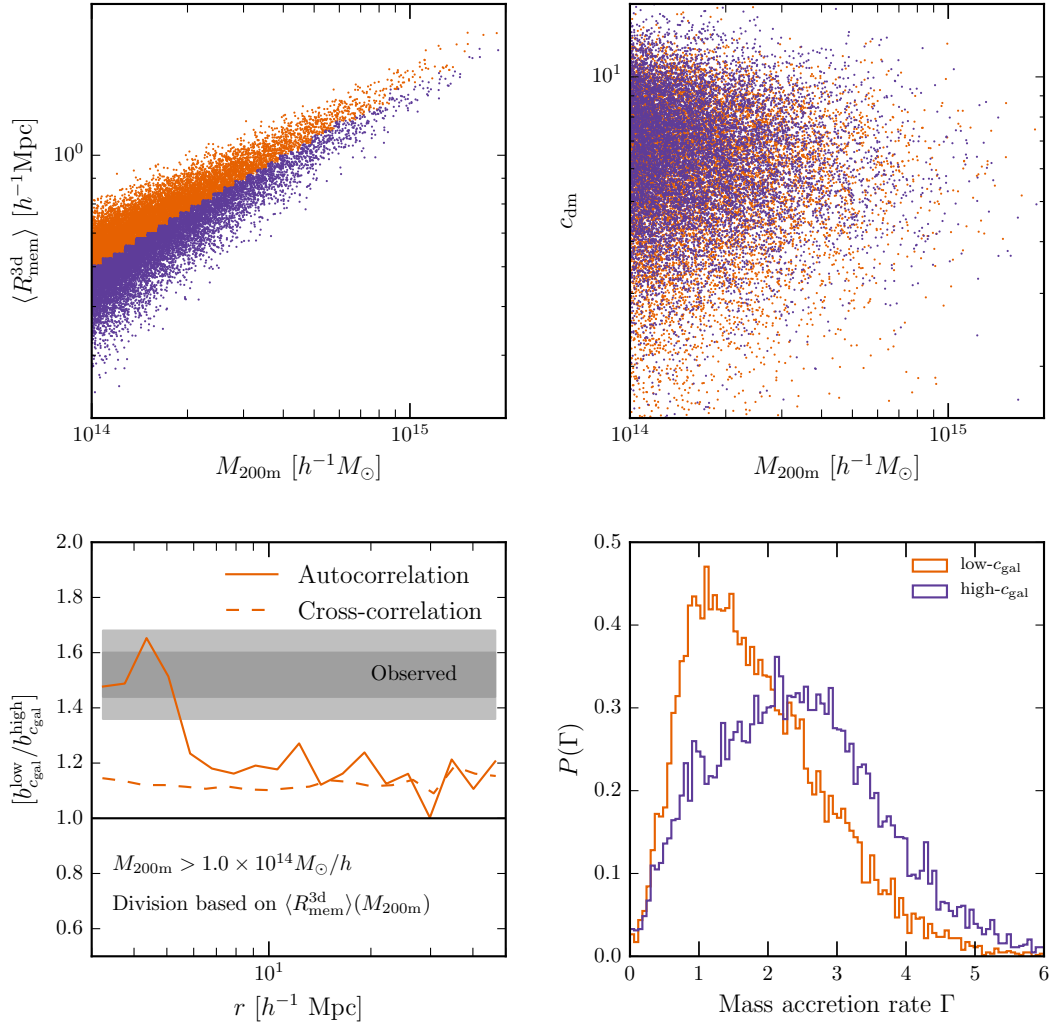


Figure 8. Expectation for halo assembly bias from simulations. *Top left panel:* The average cluster centric distance of member subhalos in cluster sized halos in MDPL2 simulation as a function of halo mass. We use the radius to divide the cluster sample into two at fixed mass. The two subsamples are shown in orange and purple colors. *Top right panel:* The same subsamples as in the top left panel but in the dark matter concentration-halo mass plane. The subhalo distribution seems to have very little correlation with the dark matter distribution. *Bottom left panel:* The ratio of the halo biases of subsamples of halos with masses $10^{14} h^{-1} M_{\odot}$ split using the average distance of their subhalos from their centers, $\langle R_{\text{mem}}^{3d} \rangle (M_{200\text{m}})$. The bias ratio obtained from cluster-cluster auto-correlations is shown with a solid line, while the dashed line corresponds to the ratio obtained from the cross-correlations of cluster-scale halos with all subhalos with $V_{\text{peak}} > 135 \text{ km s}^{-1}$ that are selected to mimic the fiducial photometric galaxies used in our analysis as in Figure 1. *Bottom right panel:* The distribution of the mass accretion rates Γ for the two subsamples.

fitting to the weak lensing surface mass density profile is expected to underestimate the virial halo mass by $\sim 10\%$ compared to the mean halo mass of clusters in the sample (Mandelbaum et al. 2005; Becker & Kravtsov 2011; Niikura et al. 2015), or $\sim 3\%$ in radius. The difference between the measured and expected splashback radii is much larger than such systematic error, and if at all will increase the inconsistency rather than decrease it. The statistical error in the weak lensing masses is less 10 percent, so even $2\text{-}\sigma$ deviations will result in only ~ 7 percent change in the expectation in the splashback radius. The errors in the weak lensing masses have also been folded in when computing the error on the observed $R_{\text{sp}}/R_{200\text{m}}$ shown in Figure 6.

4.6. Is the halo assembly bias signal consistent with expectations?

Our observational results indicate that the galaxy cluster subsample with lower concentration of member galaxies has a larger splashback radius (lower accretion rate Γ), and a larger

halo bias. Is the sense and the amplitude of the halo assembly bias signal we see consistent with expectations from cosmological simulations of cold dark matter?

Various proxies such as formation time scales of halos or their dark matter concentrations have been used in the literature to quantify halo assembly bias. The sense of the halo assembly bias effect varies depending upon the assembly proxy used. For example, Gao et al. (2005) find that halo assembly bias is strongest for low mass galaxy scale halos, and that the earliest forming halos cluster more strongly than the average for their halo masses. However, they find that the effect almost disappears on the mass scales we consider in our paper. On the contrary, when the concentration of halos is used as a proxy, halo assembly bias manifests itself at both galaxy scales and galaxy cluster scales (Wechsler et al. 2006). At galaxy scales (masses below $10^{12} h^{-1} M_{\odot}$) high concentration halos (which form earlier) have a larger halo bias, but the trend reverses on galaxy cluster scales, as expected from the

relation between mass accretion history and the curvature of initial density peaks (Dalal et al. 2008).

Li et al. (2008) explored eight different definitions of halo assembly and found that the connection between formation time and assembly bias of halos can be totally washed out or even reversed depending upon the proxy used. Member galaxy concentration has never been explored previously in the literature as a proxy for assembly history. Therefore, we use the MDPL2 simulation to explore the extent of the assembly bias expected when using it as a proxy. We ignore all observational complications, and investigate how the clustering of halos at fixed halo mass varies as a function of the concentration of the subhalo distribution belonging to the halos.

We use all isolated halos with $M_{200m} > 10^{14} h^{-1} M_{\odot}$ at $z = 0.248$ from MDPL2. This threshold in halo mass at $z = 0.248$ allows us to match the average weak lensing mass of our cluster subsamples¹⁶. To compute the average projected separation between cluster members and halo centers, we use all subhalos with $V_{\text{peak}} > 135 \text{ km s}^{-1}$, similar to the threshold used for the faintest of our photometric galaxies. We divide the sample into halves based on the 3-d cluster centric distance of the subhalos of each cluster as shown in the top left panel of Figure 8. The top right panel of the figure shows the scatter plot of dark matter concentrations of our halos given their halo masses and implies that the concentration of dark matter and concentration of subhalos are not well correlated.

The ratio of the halo bias obtained from the auto-correlation function of cluster halos in the two subsamples is shown in the bottom left panel of Figure 8 with the orange solid line, while that obtained from the cross-correlation with halos with $V_{\text{peak}} > 135 \text{ km s}^{-1}$ is shown with a dashed line. For comparison, the observed ratio between the biases of our cluster subsamples is shown with the grey shaded region. Subsample divisions based on $\langle R_{\text{mem}}^{3d} \rangle (N_{\text{sat}}^{3d})$, give very similar amplitude for this ratio at larger radius when using auto-correlations, but with weaker scale dependence. Finally, the bottom right panel shows the distributions of the mass accretion rates onto these clusters.

The halo assembly bias signal we observe in data is in the same sense, albeit stronger, than that seen in simulations¹⁷. The division in the mass accretion rates is also in the same sense as required to explain the splashback radius measurements seen in the data. These results from simulations show that it is possible to obtain samples of halos with a lower average accretion rate that have a larger clustering signal as seen in our observations.

Once projection effects are accounted for (as in Section 4.7), and the sample is divided based upon $\langle R_{\text{mem}}^{2d} \rangle (N_{\text{sat}}^{2d})$, an even smaller value for the halo assembly bias signal is obtained in simulations. Given that the strength of the halo assembly bias signal increases with halo mass, one could potentially reproduce the result by using larger mass scales in simulations. However this will further worsen the problem of the smaller splashback radius. Characterization of the halo assembly bias signal with different richness threshold samples

and theoretical investigations using larger simulations are currently ongoing and will be reported in a future publication.

4.7. Projection effects

One possible way to explain the different splashback radii and halo biases for our two cluster subsamples, could be that the two SDSS cluster subsamples in reality have different masses. The weak lensing mass estimates, taken at face value, restrict this possibility. However, the weak lensing signal is only sensitive to the projected mass distribution. The cluster subsample identification also has a very poor resolution in the line-of-sight direction. Therefore, we explore the possibility that our subsamples indeed have different 3-d masses regardless of the similarity of the weak lensing signal, and the richness of the clusters.

To address the magnitude of projection effects, we again resort to the MDPL2 simulation. We consider all halos with $M_{200m} > 10^{13} h^{-1} M_{\odot}$ as potential clusters identified from the photometric data¹⁸. We associate all halos/subhalos with $V_{\text{peak}} > 135 \text{ km s}^{-1}$ to be satellite galaxies of these potential galaxy clusters if they lie within a projected radius of R_{200m} from their centers, and have a line of sight separation less than $50 h^{-1} \text{ Mpc}$. The projected separation lengths of $\pm 50 h^{-1} \text{ Mpc}$ was obtained by considering the scatter in the colors of red sequence galaxies used to identify redMaPPer galaxy clusters, and the amount of variation of these colors as a function of redshift (see Figures 1 and 7 in Rykoff et al. 2014). If subhalos can belong to two clusters after the projection, we assign it to the most massive halo. We do not redefine or recompute the cluster centers after these projections as we expect that the redMaPPer centering algorithm is less likely to identify the galaxies in projection as centrals for the redMaPPer clusters.

In the left hand panel of Figure 9, we show the scatter plot of M_{200m}^{3d} as a function of N_{sat}^{2d} , i.e., the number of satellites associated with these cluster sized halos after the reassignment described above. To maximize the strength of projection effect, we make the extreme assumption that our two cluster subsamples select the upper and the lower half of M_{200m}^{3d} at fixed N_{sat}^{2d} . The distributions of the M_{200m}^{3d} selected in this manner are displayed in the right hand panel of Figure 9. The average halo masses corresponding to the two distributions are different by $\sim 62\%$, which implies a difference of at most $\sim 20\%$ in the radii. In contrast, the observed difference in the radii is twice as large, $\sim 40\%$. We expect the extent of projection effects to be lower, given that the average cluster centric distances for the satellites are not expected to be perfectly correlated with M_{200m}^{3d} at fixed N_{sat}^{2d} . Furthermore, due to halo assembly bias effects in simulations, the sample with larger M_{200m}^{3d} at fixed N_{sat}^{2d} turns out to have a smaller clustering signal, opposite of what is required to simultaneously explain both the different splashback radius and the sense of the assembly bias signal.

Thus, we have established that the two subsamples have splashback radii and halo biases that differ from one another by an amount that cannot be explained with the help of projection effects alone. In Appendix C, we show that both of our cluster subsamples have very similar distributions of the axis ratios of the light profiles for the most probable central

¹⁶ Note that this threshold is slightly larger than the threshold used used in Section 4.2 at $z = 0.0$. Both thresholds ensure that we match the average weak lensing mass from observations.

¹⁷ The preliminary investigations mentioned in Miyatake et al. (2015) which seemed to suggest larger assembly bias signal, were mistakenly performed using a larger mass threshold by SM. The results presented in this paper override those preliminary investigations.

¹⁸ We have chosen a slightly lower halo mass threshold for this test since projection effects can upscatter smaller halos to have a larger richness than expected for their halo masses.

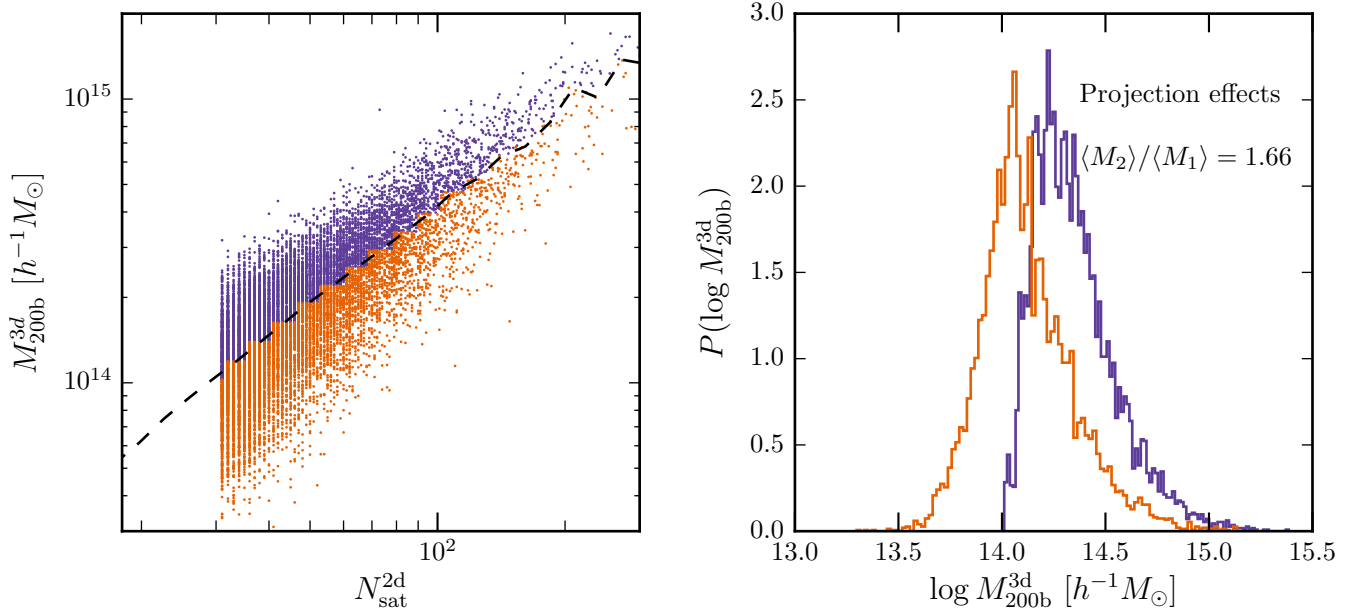


Figure 9. Estimates of projection effects. Left panel: The scatter plot of M_{200m} of halos as a function of their richness determined in projection. The richness of cluster halos in projection is computed by assigning smaller (sub)halos as satellites if they lie within a projected radius of R_{200m} and within $\pm 50 h^{-1} \text{Mpc}$ of a larger halo along the line-of-sight. To maximize projection effects, we assume the two subsamples separated by the median $M_{200m} - N_{\text{sat}}^{2d}$ relation shown by the dashed line. Right panel: The halo mass distributions of the two cluster subsamples shown in the left panel. The average halo masses are expected to be different by at most a factor of 1.66 when we maximize the projection effects.

galaxies, similar ellipticity distributions for satellite galaxies, and similar line-of-sight velocity dispersions. The similarity of these distributions is inconsistent with the trends expected, if the projection effects were behind the large magnitude of assembly bias signal or the difference in the splashback radii between the two subsamples divided by $\langle R_{\text{mem}} \rangle$.

5. DISCUSSION

In Section 3, we showed that the surface number density profiles of galaxies around redMaPPer clusters exhibit steepening characteristic of the splashback radius expected to arise in dark matter halos due to the caustic formed by matter at the first apocenter after accretion. Moreover, we showed that subsamples of the clusters of the same mass split on concentration of the galaxy distribution exhibit different splashback radii and different spatial bias.

Although comparisons with theoretical expectations presented in Section 4 show that the observed profiles and trends agree with predictions qualitatively, there are significant quantitative discrepancies. First, the observed splashback radii are significantly smaller than expected for halos corresponding to cluster masses of our sample, and second, the difference in biases of cluster subsamples is also larger than expected. Both discrepancies are very interesting because the location of the splashback radius is a result of simple gravitational dynamics and can be both robustly predicted from simulations (Diemer & Kravtsov 2014; More et al. 2015) and reproduced even in simple spherical collapse models (Adhikari et al. 2014). Likewise, halo assembly bias is expected to reflect the statistics of peaks in the initial density field from which massive cluster-sized halos form (Dalal et al. 2008). We will postpone the discussion of the larger magnitude of halo assembly bias to a future paper where we will quantify with larger simulations the extent of this discrepancy. We focus on the splashback radius discrepancy below.

We consider four possible explanations for the discrepan-

cies in the splashback radius – (a) the halo mass M_{200m} and hence the radius R_{200m} inferred from the data is larger than it really is, and this causes our measurements of R_{sp}/R_{200m} to be biased low, (b) the splashback radius of the clusters for a given accretion rate measured using galaxies is smaller than that expected from dark matter simulations, (c) the mass accretion rate onto clusters is much higher than expected for clusters of this mass, and, finally, (d) that new physics in the form of self interactions of dark matter particles results in decrease of the splashback radius. We discuss each of these possibilities in turn.

The ratio between the splashback radius of the two cluster subsamples is roughly consistent with the best case expectations from the ΛCDM simulation of the Planck cosmology (the ratio between the splashback radii corresponding to the orange and purple stars in Figure 6). Let us assume that our observational proxy results in the best case split, a very optimistic assumption, and that the weak lensing masses are overestimated. In that case, the discrepancy seen in the splashback radius for the two cluster subsamples is ~ 1.4 in radii, thus a factor of ~ 2.75 in halo masses, strongly disfavored by the small errors on the masses from weak lensing. Under this scenario, we would have uncovered a critical problem for weak lensing calibration of observable halo mass relations which are important for precision cosmological measurements using galaxy clusters. Moreover, even if we assume that the masses are overestimated for both samples, this would mean that the predicted assembly bias strength would be even lower. Such arguments thus run in the opposite sense of what is required to explain the large assembly bias signal.

If weak lensing systematics can be ruled out, one could try to explain the discrepancy if the mass accretion rate onto the clusters is normal, but the splashback radius is indeed smaller than expected. Dynamical friction on subhalos was an obvious physical effect which could cause this. However, in Sec-

tion 4.2, we have shown that the subhalos corresponding to the faintest magnitude bin we consider are not expected to experience a large amount of dynamical friction. Also, puzzlingly, in the data we do not detect a significant difference in the splashback radius with the brightness of the photometric sample used. Furthermore, future deeper surveys should be able to rule out this possibility by using even fainter galaxies. Other astrophysical possibilities include subtle biases in the photometric galaxy samples, which lead to a preferential selection of slow moving galaxies in our sample. For example, ram pressure stripping is expected to be more effective in stripping out gas and shutting down the star formation in fast moving galaxies, thus removing them preferentially from our photometric sample. Detection of the splashback radius of matter in clusters using the weak lensing signal would be able to test this possibility.

Dark matter self-interactions have long been proposed to alleviate problems on small scales in the standard cosmological model (see e.g., Spergel & Steinhardt 2000). Under certain conditions discussed below the drag force due to interactions between dark matter particles of subhalos and cluster halo could lead to loss of orbital energy by subhalos even on the first crossing, thereby reducing the splashback radius.

For isotropic elastic scattering, we do not expect dark matter self-interactions to significantly affect the splashback feature, because the upper limits on such an interaction cross-section are sufficiently stringent to ensure that most dark matter particles do not experience any scattering events during a single orbit (Gnedin & Ostriker 2001; Randall et al. 2008). Of the few subhalo particles that do scatter, most are ejected from their subhalos, since the orbital velocities of subhalos within massive hosts are typically larger than the internal escape velocities of those subhalos. Therefore we would expect evaporation of subhalo masses, without a significant drag for isotropic scattering.

On the other hand, if dark matter self-interactions are anisotropic, with large cross-sections for small angle scattering and low cross-sections otherwise, then the momentum transfer during dark matter interactions may not necessarily be large enough to ensure ejection. The small angle scattering cross-sections could then be large enough for dark matter particles to experience frequent interactions and yet obey the bounds on subhalo evaporation. The subhalos would experience a net deceleration given by

$$d = \frac{\rho(r, t)v(t)^2\sigma_{tr}}{2m_{dm}} \quad (3)$$

where $v(t)$ is the relative velocity of the subhalo, $\rho(r, t)$ is the time dependent density profile of the cluster halo, m_{dm} is the mass of the dark matter particle and σ_{tr} is the momentum transfer cross-section (Kahlhoefer et al. 2014).

We have carried out simple analytical calculations based on a spherical collapse model similar to Adhikari et al. (2014, see also Adhikari & Dalal 2016), but including a velocity-dependent drag term of the above form. We find that the momentum transfer cross-section required to reduce the splashback radius by $\approx 20\%$ can range from $1 - 20 \text{ cm}^2\text{g}^{-1}$ depending upon the pericenter of accreting halos on their first passage through the halo (More 2016b). The ambient dark matter density, the relative velocity, hence the resultant drag, reach a maximum at the pericenter. Therefore, a proper treatment of the orbital parameters of subhalos expected in the standard structure formation model is required to determine

the effects of dark matter self-interactions on the splashback radius (Jiang et al. 2014). We defer such investigations to a future paper.

Although the existing constraints on such scenarios are pretty weak, recent discovery of galaxy displacement with respect to its subhalo in one of the clusters (Harvey et al. 2015) could be a signature of self interaction (with cross section consistent with that required to explain R_{sp} discrepancy, see Kahlhoefer et al. 2015). Numerical simulations of this type of dark matter self-interaction, similar to the simulations performed for hard-sphere interactions (Elbert et al. 2015), would be required to refine the estimate of the cross-sections stated above further.

Note that even if the self interactions will ultimately not turn out to be the explanation for the splashback radius discrepancy, our analysis shows that precise measurements of galaxy distribution in clusters could provide valuable and competitive constraints on the cross section of dark matter self interaction.

If we assume that the differences in the splashback radius we find are not due to the above possibilities and we trust simple dynamics within the gravitational potential of halos, then our measurements of the smaller splashback radius would either require a different phase space structure in the outskirts of cluster halos or extreme mass accretion rates onto our cluster subsamples. The former possibility requires the velocities of material in the infall streams to be about 25-30 percent smaller. For the latter possibility, our parent sample of clusters requires values of $\Gamma \sim 4$, while the high- c_{gal} sample prefers values of $\Gamma \sim 4$. This would represent a serious challenge to the standard cosmological model. Whether modifications to gravity could achieve such values, while still obeying the bounds from galaxy cluster abundances, needs further careful evaluation.

6. SUMMARY

We have used SDSS redMaPPer galaxy clusters and photometric galaxies around them to observationally investigate the boundaries of galaxy clusters, their relation to assembly history, and to halo assembly bias on galaxy cluster scales. For this purpose, we have considered two cluster subsamples defined in Miyatake et al. (2015) which share identical richness and redshift distribution, but have different internal distributions of cluster members. These subsamples were shown to have similar halo masses as inferred from weak gravitational lensing, but have different large scale bias as measured from their large scale weak lensing and auto-correlation signals (Miyatake et al. 2015). Our results can be summarized as follows:

1. We detect the surface number density profiles of SDSS photometric galaxies with $^{0.1}M_i - 5 \log h < -19.43$ around both our cluster subsamples. The surface densities show a sharp steepening around scales of $1 h^{-1} \text{ Mpc}$.
2. We modeled the two surface density profiles using the profile advocated by Diemer & Kravtsov (2014), to infer the location of the steepening in projected and real space for both the cluster subsamples. The steepening of the surface density profiles occurs at significantly different locations for the two cluster subsamples. We interpret the steepening as the location of the splashback radius for these galaxy clusters. We attribute the difference in the splashback radii for the cluster subsamples to arise as a result of different accretion rates

onto the cluster subsamples. This implies a different assembly history for the two cluster subsamples.

3. Using simple subhalo abundance matching, we investigated whether dynamical friction affects the location of the splashback radius of subhalos expected to host our galaxies compared to that of dark matter. For the fiducial subsample, we found that the two radii should coincide within 5 percent. Observationally, the location of the steepening of the galaxy density profiles for the two cluster subsamples does not change significantly even for photometric galaxies one or two magnitudes brighter than our fiducial sample.
4. We showed that the amplitude of clustering of photometric galaxies around our two subsamples of galaxy clusters are different by 6.6σ . We have thus detected halo assembly bias, a difference in the clustering amplitude of cluster scale halos with the same mass and different assembly histories.
5. We showed that projection effects could at most cause the two subsamples to have masses different by a factor of 1.6, which is smaller than the difference required to explain the difference in the splashback radii of the two subsamples, or the different halo biases.
6. Using a large cosmological Λ CDM simulation, we have shown qualitative agreement between the trends in the splashback radius and halo assembly bias, as seen in observations. However, the splashback radii of the two cluster subsamples seem to be smaller, while the assembly bias effect larger, than naive expectations. The tests presented in the paper show that none of the systematics are large enough alone to resolve the discrepancies. If astrophysical systematics related to weak lensing, optical cluster finding, and projection effects can be conclusively ruled out, it will imply either a discrepancy between the observed accretion rates onto clusters from the expected ones, or may hint to a possible interactions in the dark matter sector, both remarkably interesting possibilities.

7. ACKNOWLEDGMENTS

Funding for the SDSS and SDSS-II has been provided by the Alfred P. Sloan Foundation, the Participating Institutions, the National Science Foundation, the U.S. Department of Energy, the National Aeronautics and Space Administration, the Japanese Monbukagakusho, the Max Planck Society, and the Higher Education Funding Council for England. The SDSS Web Site is <http://www.sdss.org/>.

The SDSS is managed by the Astrophysical Research Consortium for the Participating Institutions. The Participating Institutions are the American Museum of Natural History, Astrophysical Institute Potsdam, University of Basel, University of Cambridge, Case Western Reserve University, University of Chicago, Drexel University, Fermilab, the Institute for Advanced Study, the Japan Participation Group, Johns Hopkins University, the Joint Institute for Nuclear Astrophysics, the Kavli Institute for Particle Astrophysics and Cosmology, the Korean Scientist Group, the Chinese Academy of Sciences (LAMOST), Los Alamos National Laboratory, the Max-Planck-Institute for Astronomy (MPIA), the Max-Planck-Institute for Astrophysics (MPA), New Mexico State University, Ohio State University, University of Pittsburgh,

University of Portsmouth, Princeton University, the United States Naval Observatory, and the University of Washington.

The CosmoSim database used in this paper is a service by the Leibniz-Institute for Astrophysics Potsdam (AIP). The MultiDark database was developed in cooperation with the Spanish MultiDark Consolider Project CSD2009-00064. The MultiDark-Planck II (MDPL2) simulation has been performed in the Supermuc supercomputer at LRZ using time granted by PRACE.

We acknowledge useful discussions with Simon White, Frank van den Bosch, Andrew Hearin, Andrew Zentner, Erik Tollerud, Shigeki Matsumoto, Justin Khoury, Mark Trodden, Bhuvnesh Jain, Daisuke Nagai and Uros Seljak. MT and SM are supported by World Premier International Research Center Initiative (WPI Initiative), MEXT, Japan, and by the FIRST program ‘Subaru Measurements of Images and Redshifts (SuMIRe)’, CSTP, Japan. SM, MT and MO are also supported by Grant-in-Aid for Scientific Research from the JSPS Promotion of Science (No. 15K17600, 23340061, 26610058 and 26800093), MEXT Grant-in-Aid for Scientific Research on Innovative Areas (No. 15H05893, 15K21733, 15H05892) and by JSPS Program for Advancing Strategic International Networks to Accelerate the Circulation of Talented Researchers. HM is supported in part by Japan Society for the Promotion of Science (JSPS) Research Fellowships for Young Scientists and by the Jet Propulsion Laboratory, California Institute of Technology, under a contract with the National Aeronautics and Space Administration. AK was supported by the Kavli Institute for Cosmological Physics at the University of Chicago through grant PHY-1125897 and an endowment from the Kavli Foundation and its founder Fred Kavli. RyM acknowledges financial support from the University of Tokyo-Princeton strategic partnership grant. RM acknowledges the support of the Department of Energy Early Career Award program.

APPENDIX

A. TESTING METHODS USING SIMULATIONS

In this appendix, we use the MultiDark Planck II simulation to test our analysis methods. In particular, we show that we can recover the splashback radius for subhalos in three dimensions using the surface density profiles of subhalos around cluster scale halos.

We use all halos or subhalos in the halo catalogs with $V_{\text{peak}} > 135 \text{ km s}^{-1}$ at $z = 0$ ¹⁹. We compute the projected surface density of these subhalos around halos with masses $M > 8.5 \times 10^{13} h^{-1} M_{\odot}$, where the threshold was chosen to obtain a sample of halos which share the average weak lensing mass of the redMaPPer clusters we use in this paper²⁰. We subdivide the sample into two subsamples with different mass accretion rates, Γ , using the median mass accretion rate-halo mass relation $\Gamma(M)$.

We compute the galaxy surface densities around the resultant subsamples by projecting along the entire z -axis in the simulation. We subtract the background surface density mimicking the procedure used to compute the surface densities in the data. The errorbars on these surface densities are obtained using 125 jackknife regions in the simulation box. The resulting surface density profiles and their errorbars are shown

¹⁹ See Appendix B for our justification to choose a threshold of 135 km s^{-1} .

²⁰ This threshold halo mass is similar to the one used in Section 4.2 where we tested effects of dynamical friction using the $z = 0$ snapshot.

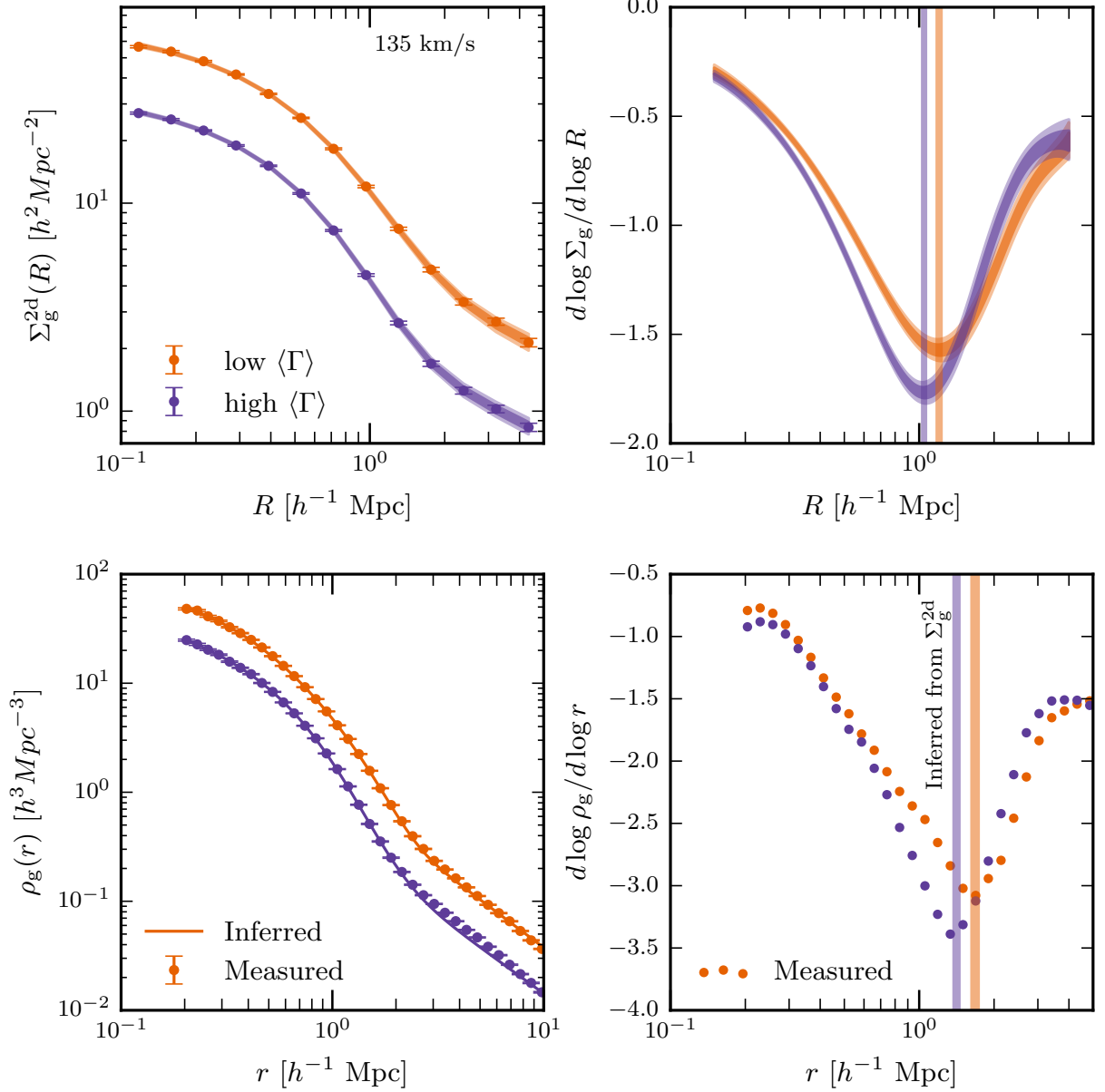


Figure 10. Tests of our methodology to determine the splashback radius of clusters. Top left panel: The subhalo surface density profiles around high and low accretion rate clusters in the MDPL2 simulation at $z=0$ are shown using purple and orange color symbols with errorbars, respectively. The data points for the low accretion rate clusters are shifted by a factor of 2.5 for clarity. The 68 and 95 percent confidence intervals based on fitting this data using the DK14 model are shown using shaded regions. Top right panel: The logarithmic derivative of the surface density profiles around the mock cluster subsamples as inferred from a model fit to the data. The vertical shaded bands correspond to the location of the steepening in two dimensions. Bottom left panel: The comparison between the three dimensional subhalo density profiles around our mock clusters, as directly measured and as inferred from the fits to the surface density profiles from the top left panel. Bottom right panel: Comparison between the logarithmic derivative of the three dimensional subhalo density profiles around our mock clusters, as directly measured and as inferred from the fits to the surface density profiles from the top left panel. The 68 percent constraints on the location of the splashback radius are shown using the shaded vertical bands. Our analytical methods can recover the location of the splashback radius in three dimensions.

in the top left panel of Figure 10. The measurements in the simulations are carried out using the same binning scheme as employed for the actual data analysis.

We fit these measured surface density profiles using the projection of the 3d DK14 density profile with the exact same priors as detailed in Section 2. The 68 and 95 percent confidence intervals on the fit are shown using the shaded regions in the top left panel of Figure 10. The inferred slope of the surface density profiles and the location of the steepest slope in two dimensions are shown in the top right panel.

The points in the bottom left panel correspond to the three

dimensional density profiles of these subhalos as measured from the simulation directly. The solid lines are used to indicate the three dimensional subhalo density profiles as predicted by the best fit to the subhalo surface density profiles in the upper panels. Finally, in the bottom right panel we compare the inferred and measured logarithmic slopes of the three dimensional density profiles. This test shows that our analysis methods can reproduce the location of the splashback radius by fitting the two dimensional density profiles of subhalos in the simulations.

B. ABUNDANCE MATCHING CONSTRAINTS ON THE SUBHALOS HOSTING PHOTOMETRIC GALAXIES

We use the surface number density distribution of photometric galaxies around our cluster subsamples to detect the splashback radius. In this appendix, we use a simple subhalo abundance matching technique to determine the properties of subhalos hosting the photometric galaxies we use in this paper. The left hand panel of Figure 11, shows the cumulative abundance of galaxies, based on the Schechter function fit to the $^{0.1}i$ -band luminosity function for SDSS galaxies obtained by Blanton et al. (2003)²¹.

We k-correct the absolute magnitude limits of the photometric galaxies we use, as well as correct them for the luminosity evolution of galaxies (e -correction) from $z = 0.24$, the median redshift of our cluster subsamples, to $z = 0.1$. We approximate the k-correction as

$$^{0.1}k(z) = -2.5 \log_{10} \left[\frac{z + 1.3}{1.1(0.1 + 1.3)} \right], \quad (\text{B1})$$

found by fitting the k-correction as a function of redshift using the SDSS main sample of spectroscopic galaxies. We have ignored the residual color dependent scatter in this relation. These $k + e$ corrected magnitude limits for our photometric subsamples are shown with vertical dashed lines, while the horizontal dashed lines show their cumulative abundances. We do not assume any scatter between V_{peak} and magnitude, to obtain a limit on the maximum effect that dynamical friction can have, and match these abundances directly to those of subhalos as a function of V_{peak} . The result of this simple subhalo abundance matching exercise is shown in the right hand panel of Figure 11.

The abundance matching implied that the subhalos hosting our fiducial subsample of photometric galaxies approximately correspond to subhalos with $V_{\text{peak}} > 135 \text{ km s}^{-1}$, while the brighter subsamples correspond to subhalos with $V_{\text{peak}} > 175 \text{ km s}^{-1}$ and $V_{\text{peak}} > 280 \text{ km s}^{-1}$, respectively. In Section 4.2, these abundance matching constraints are used to explore how dynamical friction is expected to affect the location of the splashback radius for our subsamples.

C. ADDITIONAL INVESTIGATIONS REGARDING PROJECTION AND HALO ORIENTATION EFFECTS

Galaxy cluster halos are expected to be triaxial, and if the major axis of clusters in one of our subsamples were preferentially aligned along the line-of-sight, we could overestimate the halo mass of that particular subsample (see e.g., Oguri et al. 2005). We have performed the following tests to evaluate such possibility. Any attempts to explain the halo assembly bias signal based on projection or orientation effects, should also satisfy these observational constraints.

We have utilized the spectroscopic coverage of the SDSS-DR12 LOWZ galaxy sample to investigate the velocity distributions of such galaxies around our cluster subsamples. If one of our subsamples is heavily affected by projection effects, then the velocity distributions around the two subsamples should reveal differences. The redMaPPer cluster catalog contains spectroscopic redshifts for 3037 (2830) most probable central galaxies in the high- (low-) c_{gal} subsamples. We show the $P(\Delta V)$ distribution of all spectroscopic galaxies within a projected radius of $R_{200\text{m}}$ of the cluster center in the

²¹ The notation $^{0.1}i$ stands for magnitude in the i -band k-corrected to $z = 0.1$.

left hand panel of Figure 12. We find very little evidence, if any, of a difference between the two distributions.

The photometric major axis of central galaxies has been reported to have a preferential alignment with the major axis of the dark matter halo, albeit with a reasonable scatter (see e.g., Evans & Bridle 2009; Oguri et al. 2010, 2012). If one of our subsamples (the high- c_{gal} subsample) had major axis which were preferentially aligned with the line-of-sight, we expect the BCG ellipticities of that sample to be rounder than the other. In the middle hand panel of Figure 12, we show the axis ratio distributions of the light distribution in various SDSS bands as reported by the SDSS photometric pipeline, of the most probable central galaxies in our two subsamples. These axis ratios were computed by fitting a deVaucouleurs profile to the two-dimensional image of each object in each band (Stoughton et al. 2002). We do not see any strong evidence for a difference in the axis ratios of the most probable central galaxies between the two cluster subsamples.

The satellite galaxy distribution is also expected to have a preferential alignment with the major axis of the dark matter halo (see e.g., Zentner et al. 2005; Kang et al. 2007). We compute the second moment of the projected satellite galaxy distribution around our cluster subsamples using the membership probabilities of all member galaxies as reported in the redMaPPer catalog. We use these second moments to compute the major and minor axis, and their axis ratios, around the most probable central galaxies. In the right hand panel of Figure 12, we show the axis ratio distributions of the member galaxy distributions. Again we see very little difference between the two cluster subsamples.

D. MAGNIFICATION DUE TO CLUSTERS

The background density of photometric galaxies behind clusters is expected to be different from the background density around random points due to magnification effects by galaxy clusters. We consider a simple estimate of this effect based on the weak lensing mass estimate of our clusters. The magnification changes the number counts in two ways: firstly, fainter galaxies can now enter our sample after being magnified by the cluster, secondly, the background galaxies occupy a smaller solid angle behind the cluster than in the absence of magnification.

For simplicity, we assume that all our clusters are located at the median redshift of our subsample. We assume that background galaxies follow the luminosity function presented by Blanton et al. (2003). The number of galaxies that will be observed at a projected distance R from the cluster is then given by

$$N(R|z_l, z_s) = \int dz_s \frac{dV}{dz_s} \frac{1}{\mu(R|z_l, z_s)} \Phi(M < M'_{\text{max}}|z_s) \quad (\text{D1})$$

where μ denotes the magnification due to the cluster at a projected distance R , and

$$M'_{\text{max}} = M_{\text{max}} - 5.0 \log_{10}(D_l[z_s]/D_l[z_l]) + 2.5 \log_{10} \mu(R|z_l, z_s). \quad (\text{D2})$$

Here M_{max} corresponds to a maximum absolute magnitude for galaxies that end up in our subsample. In the paper, we have considered three different thresholds, $M_{\text{max}} - 5 \log h = -19.43, -20.43$ and -21.43 . The above equation accounts for the fact that we have assumed the redshift of the photometric galaxies to be equal to that of the lens redshift while converting their apparent magnitudes to absolute magnitudes. We additionally k+e correct M_{max} to $z = 0.1$ as the luminosity

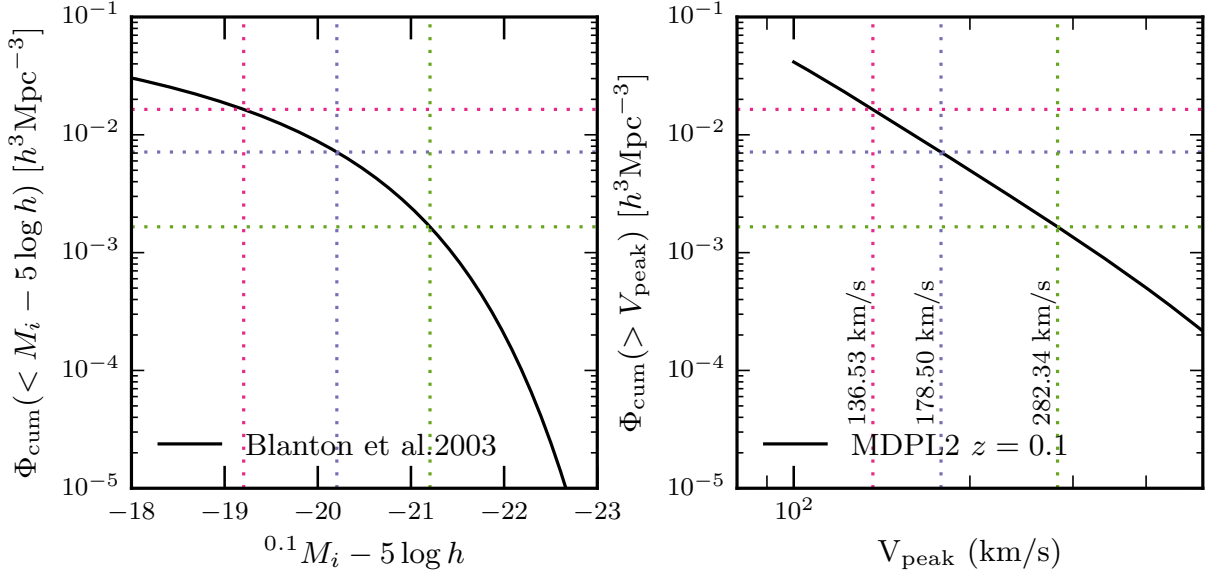


Figure 11. Left panel: The cumulative abundance of SDSS galaxies as a function of their i -band magnitude from Blanton et al. (2003). The dotted vertical lines correspond to the magnitude limits of our photometric samples of galaxies k -corrected and evolution corrected to $z = 0.24$, the median redshift of the sample. The horizontal lines give the cumulative abundances. Right panel: The cumulative abundances of subhalos in MDPL2 simulation as a function of V_{peak} . The horizontal dotted lines are the cumulative abundances of our photometric samples taken from the left panel, while the vertical dashed lines give the V_{peak} thresholds corresponding to our photometric subsamples. These V_{peak} thresholds are used to test dynamical friction effects on the location of the splashback radius (see Figure 7).

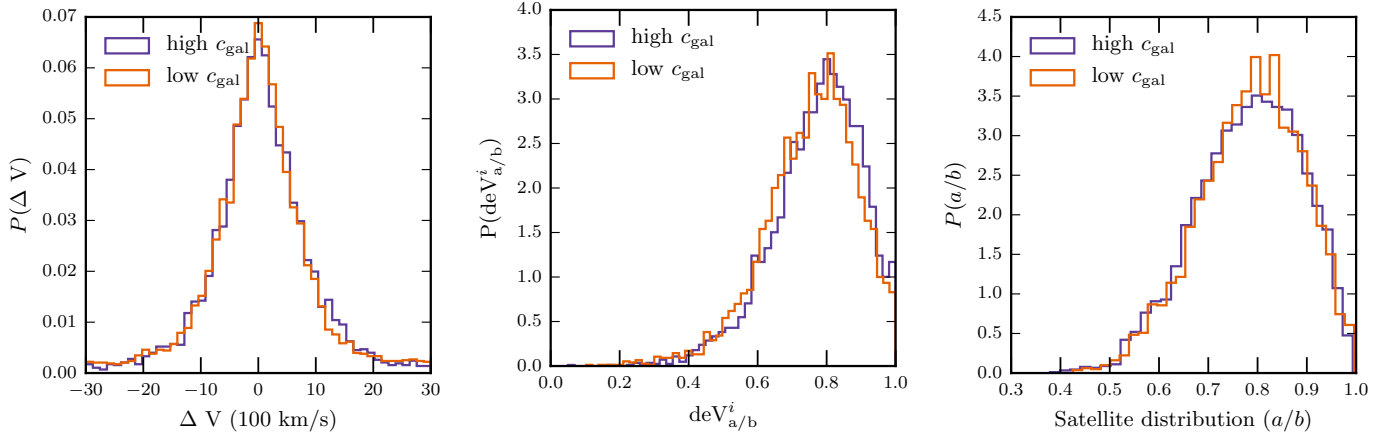


Figure 12. Left panel: The distributions of line-of-sight velocities of spectroscopic galaxies from SDSS around most probable redMaPPer central galaxies in the two subsamples. Middle panel: The distributions of the axis ratios of the light profiles in the i band for the most probable centrals in the two cluster subsamples are shown. Right panel: The distributions of the axis ratios of the satellite distributions around the most probable centrals in the two cluster subsamples are shown. We do not see a large differences between our two cluster subsamples for any of these statistics.

function we use is based on such k + e corrected magnitudes.

In Figure 13, we plot the ratio between the number counts obtained by using Eq D1 with μ obtained for a halo of mass M_{200m} that matches the weak lensing estimate for our cluster subsamples. We see that due to the magnification of our clusters, we should be underestimating our background at smaller radii by 5 to 10 percent, depending upon the photometric sample under consideration, although the corrections to the background near the splashback radii is about 1 percent. To check for the systematic effect arising from magnification effects, we multiply the number counts around random points by this ratio before subtracting them from the number of galaxies around our cluster subsamples. Note that this is a conservative estimate of the effect, because this factor should only be applied to the background galaxies, where as the number

of galaxies around random points also consist of foreground galaxies. We have confirmed that the location of the splashback radius is insensitive to such a change. If at all it is expected to be lowered by such a change, given that we are underestimating the background.

REFERENCES

Adhikari, S., & Dalal, N. 2016, in preparation
 Adhikari, S., Dalal, N., & Chamberlain, R. T. 2014, J. Cosmology Astropart. Phys., 11, 19
 Aihara, H., et al. 2011, ApJS, 193, 29
 Bardeen, J. M., Bond, J. R., Kaiser, N., & Szalay, A. S. 1986, ApJ, 304, 15
 Becker, M. R., & Kravtsov, A. V. 2011, ApJ, 740, 25
 Behroozi, P. S., Wechsler, R. H., & Wu, H.-Y. 2013, ApJ, 762, 109
 Bertschinger, E. 1985, ApJS, 58, 39
 Blanton, M. R., et al. 2003, ApJ, 592, 819

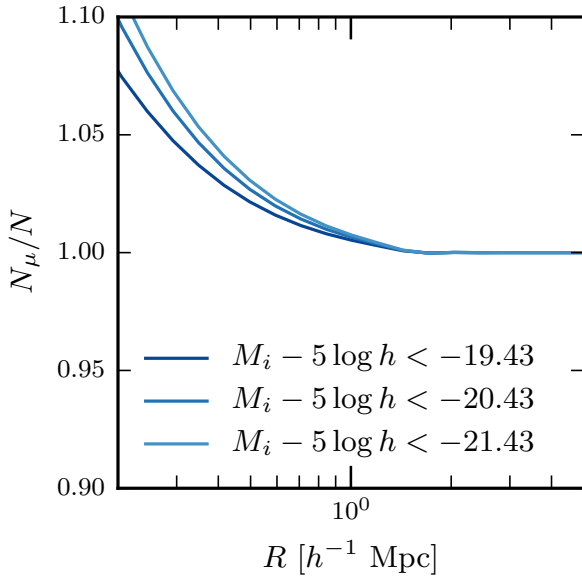


Figure 13. Magnification effects on the background estimation: The ratio of the number counts of background galaxies behind a cluster compared to that around random points, for the three different photometric samples we use in the paper. On scales of interest for the splashback radius the corrections to the background estimate are at the percent level. We have checked that the splashback radius estimates are not affected by such small changes to the background.

Dalal, N., White, M., Bond, J. R., & Shirokov, A. 2008, *ApJ*, 687, 12
 Diemer, B., & Kravtsov, A. V. 2014, *ApJ*, 789, 1
 Elbert, O. D., Bullock, J. S., Garrison-Kimmel, S., Rocha, M., Oñorbe, J., & Peter, A. H. G. 2015, *MNRAS*, 453, 29
 Evans, A. K. D., & Bridle, S. 2009, *ApJ*, 695, 1446
 Fillmore, J. A., & Goldreich, P. 1984, *ApJ*, 281, 1
 Foreman-Mackey, D., Hogg, D. W., Lang, D., & Goodman, J. 2013, *PASP*, 125, 306
 Gao, L., Navarro, J. F., Cole, S., Frenk, C. S., White, S. D. M., Springel, V., Jenkins, A., & Neto, A. F. 2008, *MNRAS*, 387, 536
 Gao, L., Springel, V., & White, S. D. M. 2005, *MNRAS*, 363, L66
 Gao, L., & White, S. D. M. 2007, *MNRAS*, 377, L5
 Gnedin, O. Y., & Ostriker, J. P. 2001, *ApJ*, 561, 61
 Goodman, J., & Weare, J. 2010, *Commun. Appl. Math. Comput. Sci.*, 5, 65
 Harvey, D., Massey, R., Kitching, T., Taylor, A., & Tittley, E. 2015, *Science*, 347, 1462
 Hearin, A. P., Watson, D. F., & van den Bosch, F. C. 2014, *ArXiv e-prints*
 Hikage, C., Mandelbaum, R., Takada, M., & Spergel, D. N. 2013, *MNRAS*, 435, 2345
 Jiang, F., & van den Bosch, F. C. 2014, *ArXiv e-prints*
 Jiang, L., Helly, J. C., Cole, S., & Frenk, C. S. 2014, *MNRAS*, 440, 2115
 Kahlhoefer, F., Schmidt-Hoberg, K., Frandsen, M. T., & Sarkar, S. 2014, *MNRAS*, 437, 2865

Kahlhoefer, F., Schmidt-Hoberg, K., Kummer, J., & Sarkar, S. 2015, *MNRAS*, 452, L54
 Kaiser, N. 1984, *ApJL*, 284, L9
 Kang, X., van den Bosch, F. C., Yang, X., Mao, S., Mo, H. J., Li, C., & Jing, Y. P. 2007, *MNRAS*, 378, 1531
 Klypin, A., Yepes, G., Gottlöber, S., Prada, F., & Hess, S. 2014, *ArXiv e-prints*
 Kravtsov, A. V., & Borgani, S. 2012, *ARA&A*, 50, 353
 Li, Y., Mo, H. J., & Gao, L. 2008, *MNRAS*, 389, 1419
 Lin, Y.-T., Mandelbaum, R., Huang, Y.-H., Huang, H.-J., Dalal, N., Diemer, B., Jian, H.-Y., & Kravtsov, A. 2015, *ArXiv e-prints*
 Mandelbaum, R., et al. 2005, *MNRAS*, 361, 1287
 Miyatake, H., More, S., Takada, M., Spergel, D. N., Mandelbaum, R., Rykoff, E. S., & Rozo, E. 2015, *ArXiv e-prints*
 Mo, H. J., & White, S. D. M. 1996, *MNRAS*, 282, 347
 More, S. 2016a, in preparation
 —. 2016b, in preparation
 More, S., Diemer, B., & Kravtsov, A. V. 2015, *ApJ*, 810, 36
 Navarro, J. F., Frenk, C. S., & White, S. D. M. 1996, *ApJ*, 462, 563
 Niikura, H., Takada, M., Okabe, N., Martino, R., & Takahashi, R. 2015, *PASJ*
 Oguri, M., Bayliss, M. B., Dahle, H., Sharon, K., Gladders, M. D., Natarajan, P., Hennawi, J. F., & Koester, B. P. 2012, *MNRAS*, 420, 3213
 Oguri, M., & Hamana, T. 2011, *MNRAS*, 414, 1851
 Oguri, M., Takada, M., Okabe, N., & Smith, G. P. 2010, *MNRAS*, 405, 2215
 Oguri, M., Takada, M., Umetsu, K., & Broadhurst, T. 2005, *ApJ*, 632, 841
 Patej, A., & Loeb, A. 2015, *ArXiv e-prints*
 Randall, S. W., Markevitch, M., Clowe, D., Gonzalez, A. H., & Bradač, M. 2008, *ApJ*, 679, 1173
 Rines, K., Geller, M. J., Diaferio, A., & Kurtz, M. J. 2013, *ApJ*, 767, 15
 Rozo, E., Rykoff, E. S., Becker, M., Reddick, R. M., & Wechsler, R. H. 2014, *ArXiv e-prints*
 Rykoff, E. S., et al. 2014, *ApJ*, 785, 104
 —. 2016, *ArXiv e-prints*
 Schlegel, D. J., Finkbeiner, D. P., & Davis, M. 1998, *ApJ*, 500, 525
 Sheth, R. K., Mo, H. J., & Tormen, G. 2001, *MNRAS*, 323, 1
 Sheth, R. K., & Tormen, G. 2004, *MNRAS*, 350, 1385
 Skibba, R. A., van den Bosch, F. C., Yang, X., More, S., Mo, H., & Fontanot, F. 2011, *MNRAS*, 410, 417
 Spergel, D. N., & Steinhardt, P. J. 2000, *Physical Review Letters*, 84, 3760
 Stoughton, C., et al. 2002, *AJ*, 123, 485
 Tinker, J. L., George, M. R., Leauthaud, A., Bundy, K., Finoguenov, A., Massey, R., Rhodes, J., & Wechsler, R. H. 2012, *ApJL*, 755, L5
 Tinker, J. L., Robertson, B. E., Kravtsov, A. V., Klypin, A., Warren, M. S., Yepes, G., & Gottlöber, S. 2010, *ApJ*, 724, 878
 Tully, R. B. 2015, *AJ*, 149, 54
 Umetsu, K., Broadhurst, T., Zitrin, A., Medezinski, E., & Hsu, L.-Y. 2011, *ApJ*, 729, 127
 Vogelsberger, M., Mohayaee, R., & White, S. D. M. 2011, *MNRAS*, 414, 3044
 Wechsler, R. H., Zentner, A. R., Bullock, J. S., Kravtsov, A. V., & Allgood, B. 2006, *ApJ*, 652, 71
 Yang, X., Mo, H. J., & van den Bosch, F. C. 2006, *ApJL*, 638, L55
 Zentner, A. R., Kravtsov, A. V., Gnedin, O. Y., & Klypin, A. A. 2005, *ApJ*, 629, 219